Supplemental Appendix

Appendix A. Discussion on the genetic basis of red color pattern variation in *Heliconius*

A recent, prevailing model within *Heliconius* biology has been that the major red color pattern elements, including the dennis (basal forewing triangle), rays (intervenous hindwing stripes), and postman forewing band, are determined by modular cis-acting enhancers of the gene *optix* (1–4). Under this model, each enhancer is sufficient to activate the presence of a single red color pattern element, and the hypothetical placement of a modular enhancer into a morph lacking that pattern should be sufficient to induce the new phenotype. This model has, in turn, led to the "enhancer shuffling" hypothesis, which dictates that *Heliconius* color patterns have evolved through recombination between pattern element-specific modular enhancers.

The modular enhancer model has received significant attention despite the fact that it is almost entirely speculative–there have been no functional assays of putative modular enhancer elements, and previous data can be interpreted as supporting alternative models. Based on previously published data, as well as new findings in this study, we propose that the evolution of epistasis, in part through gain and/or loss of cis-regulatory silencers around *optix*, is likely an important mechanism of color pattern evolution in *Heliconius*. We coin the term "enhancer shuttering" to describe this model, in reference to Gilbert (5) who proposed an epistatic repression model over 15 years ago using the metaphor of "windows" and "shutters".

Here we outline several lines of evidence that challenge the modular enhancer shuffling model and/or favor the epistatic shuttering model, especially in *Heliconius erato*:

1. Crosses showing red color pattern segregation have not yet provided evidence for modularity at the *optix* locus.

The most comprehensive and frequently cited study of color pattern genetics in *Heliconius erato* is by Sheppard et al. (6), who studied multiple crosses of both postman and radiate morphs to identify the Mendelian loci controlling color patterns. Interestingly, Sheppard et al. were not able to achieve a single recombinant between the dennis and rays phenotypes, and referred to these morphs as simply having the "radiate" (*R*) phenotype, which is consistent with our result of pleiotropic CREs driving *optix* expression in both dennis and rays (Fig. 3). A single *H. erato* race, *H. e. amalfreda*, which contains only the dennis phenotype while lacking rays, was also studied extensively by Sheppard et al. As with the radiate phenotype, they were similarly unable to identify a dennis-only locus (*D*) separate from the rays phenotype in crosses, and referenced the dennis phenotype as an alternate allele of the radiate *R* locus, matching our prediction that subsequent evolution has occurred in this derived morph. Subsequent *H. erato* crosses using the Amazonian radiate races, such as those in (7), were also unable to separate the dennis from the rays phenotypes, nor were earlier crosses, such as those in Turner and Crane (8). Notably, the *Y* locus, which controls the color (red or yellow) of the forewing band, has also never been found to recombine with either the dennis or rays phenotypes, and only appears with these two phenotypes in heterozygotes.

2. Crosses show extensive evidence for epistatic regulation of *optix*-positive red color patterns

Multiple lines of evidence point to epistasis playing a primary role in the generation of the dennis and rays phenotypes in both *H. erato* and *H. melpomene.* Previous study of crosses from pure parental phenotypes (e.g. (6)) and natural hybrids from a hybrid zone in Peru (9) have shown that alleles of other major color pattern loci are epistatic with the red color pattern phenotypes. Sheppard et al. (6) note that in *H. melpomene* the *N* locus, which controls yellow on the forewing, is epistatic on the red forewing band. Similarly, Mallet (9) adds that Peruvian homozygotes for one allele of *Sd* in *H. erato*, which maps to the gene *WntA*, show reduced or absent rays in the region where the yellow hindwing bar of postman races would be present. This effect of *Sd* alleles on both dennis and rays phenotypes in *H. erato* from French Guiana is seen in Shaak and Counterman (10), where *Dd* / *SdSd* (i.e. heterozygous for dennis and rays, homozygous for Sd) shows a greatly reduced dennis phenotype and partial loss of rays at the base of the hindwing relative to *Dd* / *sdsd*. It is also shown in (9), amongst others, that the *Cr* locus controlling the presence/absence of a yellow hindwing bar is varyingly dominant over the rays phenotype in this region of the hindwing, indicating complex epistatic interactions between the loci *Sd* (i.e. *WntA)*, *Cr* (i.e. *cortex*), and *D* (i.e. *optix*).

3. Wild hybrids cannot distinguish between epistasis or modularity

Of the thousands of butterflies collected from hybrid zones, two rare *H. erato* phenotypes have been collected (with photographs) from the wild with a lack of the dennis phenotype and showing only a partial loss of the rays (9). In both cases (one shown in Mallet (9), the other found in Ackery & Smiles (11), collected in Peru and Boliva) these individuals appear to carry only partial rays phenotypes—inconsistent with a rays enhancer module—and appear to have at least one additional hybrid parent (the Peruvian sample carries alleles similar to those of *H. e. favorinus, H. e. amphitrite*, and a rayed race), suggesting that epistatic interactions may explain some variation in the dennis and rays phenotypes not seen in simple hybrids. This is supported by the rarity of these morphs: Mallet found a single individual out of 1571 collected butterflies, while the other is the only specimen of its type in the British Museum. Similar hybrids in the British Museum collection show partial loss of both dennis and rays phenotypes, which is more consistent with epistasis than modularity, as does a hybrid specimen from French Guiana found in the Cornell collection (Appendix Fig. 1). Interestingly, one of the parental morphs for the hybrid individual found

Appendix Figure 1. **Hybrid *H. erato* from French Guiana.** Putative hybrid between *H. e. erato* and *H. e. hydara* displaying reduced dennis and rays phenotypes indicative of epistasis rather than modularity.

in the British museum collection (*H. e. phyllis*) displays a yellow stripe phenotype in the middle of the dennis element that appears to switch between yellow and red, independent of both the dennis and forewing red band elements, indicating that the genetics of red pattern elements in this region is not entirely similar to that of the Amazonian and Central American morphs. While these rare hybrids suggest epistasis, without knowledge of the genetic background for these hybrids, it is difficult to infer the genetic basis of partial pattern elements and they do not explicitly provide support for either modular enhancers or epistasis.

As noted by Turner (12), a region in Suriname and French Guiana of hybridization between three morphs contains phenotypes for dennis only (*H. e. amalfreda*), dennis and rays together (*H. e. erato*), and a red forewing band (*H. e. hydara*). Turner considers the case of two separate alleles for dennis and rays in this region, which would predict the presence (though potentially rare) of natural recombinants separating the dennis and ray phenotypes, and rejects this notion due to the complete lack of observation of the rays phenotype alone or in the presence of only the red forewing band in the natural population. Because of this observation, Turner rejected the hypothesis of modular loci for the dennis and rays elements in favor of a single genetic architecture with allelic variation within the region.

4. Sequence association studies consistently highlight multiple loci, and thus cannot rule out epistasis to explain red color pattern variation.

DNA sequence comparisons have been cited to support the modular enhancer shuffling model in *H. erato* (3). In this case, the authors started with an assumption of modularity and used SNP variation at hybrid zones to identify loci around *optix* that associate with different red color patterns. Identification of the loci associated with dennis and rays assumed that all races would differ at the same sites, and thus relied on taking the intersection of all population divergence scans at radiate hybrid zones to identify the few loci associated with all differences between radiate and alternate morphs. This was combined with phylogenetic weighting across multiple species with variable hindwing and forewing red color patterns to narrow association intervals to relatively small genomic regions. These narrow regions were interpreted as “modules” for a single species, but more likely reflect the intersection of loci between all species and morphs analyzed.

Two key studies have used genome wide association mapping to identify the genetic basis of phenotypic variation (7, 13). In both cases association of both red and black wing elements consistently showed simultaneous associations above the significance threshold for both the *optix* locus and at least one other major color pattern gene expressed prior to *optix* during development, in particular *WntA* and *cortex*. Additionally, a recent study of crosses between *H. m. aglaope* (dennis and rays phenotype) and *H. m. meriana* (dennis phenotype only), found that while the presence or absence of rays between the two morphs mapped to chromosome 18 (*optix*), quantitative analysis of the amount of red in the rays region mapped to three loci on chromosomes 1, 12, and 18, again indicating epistasis (4). Variation in the forewing band area similarly mapped to multiple chromosomes, including all chromosomes containing all three major color pattern genes. In sum, these association studies do not support a model where *optix* acts alone in natural populations to determine regional variation of red color patterns, and

are more consistent with a model where upstream genes including *WntA* and *cortex* contribute to establishing the red color pattern domain.

6. Interspecific hybrids show novel red patterns, favoring epistasis instead of modular enhancers.

Consistent with the epistatic interactions identified in *H. melpomene* and *H. erato* crosses, interspecific hybrids, primarily in the *H. melpomene* clade, show a substantial degree of epistatic interaction. Multiple natural hybrids of *H. m. melpomene* and *H. n. superioris*, and also *H. m. meriana* and *H. n. superioris* (14) have been observed where two putative "rays" recessive homozygote parental phenotypes have hybridized to form offspring with rays or a ray-like phenotype, suggesting that rays can be gained or lost solely through changes in the genetic background, without novel *optix* enhancer alleles (See Appendix Fig. 2, below).

Appendix Figure 2. **Interspecific hybrids from Mallet et al. 2007.** *H. m. meriana* and *H. n. superioris* (top) and *H. m. melpomene* and *H. n. superioris* (bottom) hybrids show a dennis and rays-like phenotype despite absence of rays in both parental phenotypes and black pigmentation within the dennis region. Images reprinted from ref. 14, which is licensed under CC BY 2.0.

Similar evidence for epistasis on the dennis phenotype is found (amongst others) in the same hybrids, where a patch of black on the forewing of *H. n. superioris* found within the dennis region of the forewing is inherited by the hybrid offspring despite the dominance of the dennis phenotype in *H. melpomene* crosses. Observation of natural variation in *H. elevatus* morphs, which are part of the previously identified *H. melpomene* clade radiate introgression group, also supports epistasis of black elements on the dennis pattern. Though less well studied, black on the forewing in the same location as the *H. erato Sd*

and *H. melpomene N* / *Ac* phenotypes appears to control the distal extent of the dennis pattern. Overall, these types of data show that changes in the epistatic trans-regulatory landscape are sufficient to cause the appearance of new red color patterns without introducing new *optix* enhancers.

7. Knockouts of the *WntA* color patterning gene are sufficient to generate novel *optix*-positive color patterns without introduction of novel *optix* enhancers.

As described in the main text, deletion of *WntA*, a ligand-encoding gene that maps to the mendelian *Sd* and *Ac* loci in *H. erato* and *H. melpomene* respectively (15), causes a dramatic expansion of red color patterns on the forewing, essentially generating a new dennis pattern *de novo*. This shows that a change in the genetic background alone is sufficient to induce red patterning in the dennis region of the forewing, completely without introduction of new *optix* enhancers. These results also show that repression of *optix* by *WntA* is sufficient for modulating red coloration across the entire dennis pattern. As described above in Point 4, this is particularly compelling because *WntA* and *optix* consistently show correlated association profiles in genome wide association studies (7, 13). Together, in situ data, genetic crosses, association studies, and knockouts all support *WntA* as a classical shutter gene sensu Gilbert (5).

8. Knockouts of some *optix* CREs cause expansion of red color patterns, supporting an epistatic repression model.

As described in the main text, we have recovered CRE deletion mutants in both *H. erato* (*obs214*) and *H. melpomene* (*obs214m*) that result in expansion of red color patterns into normally black regions of the wing (Fig. 6). The fact that the presumptive expression domain of *optix* expands in response to CRE deletion suggests that these non-coding elements have silencer functionality. This, in turn, necessitates an epistatic interaction that would normally repress *optix*, which is lost when the silencer is deleted.

Enhancer shuttering: red color pattern evolution in *Heliconius* occurs through modulation of epistasis

In sum, the lack of definitive evidence for genetic modularity between dennis and rays elements across thousands of individuals from hundreds of crosses, multiple lines of evidence supporting epistasis, and our results showing interdependence, pleiotropy, and silencer activity of *optix* CREs in a radiate morph (*H. e. lativitta*) leads us to propose that enhancer shuttering is a primary driver of intraspecific red color pattern evolution in *Heliconius erato*. More explicitly, our model predicts that sequence variation at different *optix* CREs modulates repression via upstream factors (i.e. shutter genes such as *WntA*). The effect of these repressors on *optix* expression is essential for carving out the final expression domain of *optix* from a broader area that is determined through collective activity of multiple *optix* enhancers (a “window” sensu Gilbert). As described above, and in the main text, this model explains our results and accommodates results from previous sequence association studies. Epistasis also accounts for the observation that in all cases where natural morphs have only dennis (*H. e. amalfreda* and *H. m. meriana*) or rays (*H. timareta timareta*), it is always the apparent loss of a red pattern from an individual otherwise similar to neighboring morphs with both dennis and rays. This could be explained simply by repression of *optix* by *WntA*, for instance.

While epistatic enhancer shuttering is a useful explanatory model that accommodates the data we have on hand, there are still many unresolved questions that need to be addressed with functional work. One major outstanding set of questions concerns how *optix* CREs interact to prepattern the *optix* window, to what extent the window itself varies between species and populations, and what the trans-regulatory determinants of the window are. We also need more detailed work to pinpoint causative sequence variants that alter enhancer and silencer activities of *optix* CREs. In any case, the enhancer shuttering model allows us to generate a new set of predictions that can be tested in a next generation of experiments that we hope will include more precise functional genomic, genome editing, and reporter construct approaches

References for Appendix A:

1. Merrill RM, et al. (2019) Genetic dissection of assortative mating behavior. *PLOS Biol* 17(2):e2005902.
2. Wallbank RWR, et al. (2016) Evolutionary novelty in a butterfly wing pattern through enhancer shuffling. *PLOS Biol* 14(1):e1002353.
3. Van Belleghem SM, et al. (2017) Complex modular architecture around a simple toolkit of wing pattern genes. *Nat Ecol Evol* 1(3):0052.
4. Morris J, et al. (2019) The genetic architecture of adaptation: convergence and pleiotropy in *Heliconius* wing pattern evolution. *Heredity (Edinb)*. doi:10.1038/s41437-018-0180-0.
5. Gilbert LE (2003) *Adaptive novelty through introgression in Heliconius wing patterns: Evidence for shared genetic "tool box" from synthetic hybrid zones and a theory of diversification*. in Ecology and Evolution Taking Flight: Butterflies as Model Systems, C. L. Boggs, W. B. Watt, P. R. Ehrlich, Eds. (University of Chicago Press), pp. 281-318.
6. Macdonald SP, et al. (1985) Genetics and the evolution of muellerian mimicry in heliconius butterflies. *Philos Trans R Soc London B, Biol Sci* 308(1137):433–610.
7. Papa R, et al. (2013) Multi-allelic major effect genes interact with minor effect QTLs to control adaptive color pattern variation in *Heliconius erato*. *PLoS One* 8(3):e57033.
8. Turner JRG, Crane J (1962) The genetics of some polymorphic forms of the butterflies *Heliconius melpomene linnaeus* and *Heliconius erato linnaeus*. I. Major genes. *Zool New York Zool Soc* 47(13):141–152.
9. Mallet J (1989) The genetics of warning colour in Peruvian hybrid zones of *Heliconius erato* and *H. melpomene*. *Proc R Soc London B Biol Sci* 236(1283):163–185.
10. Shaak SG, Counterman BA (2017) High warning colour polymorphism in Heliconius hybrid zone roosts. *Ecol Entomol* 42(3):315–324.
11. Ackery PR, Smiles RL (1976) An illustrated list of the type-specimens of the Heliconiinae (Lepidoptera, Nymphalidae) in the British Museum (Natural History). *Bull Br Mus Nat Hist (Ent)* Vol. 32(5).
12. Turner JRG (1971) Two thousand generations of hybridisation in a *Heliconius* butterfly. *Evolution (N Y)* 25(3):471–482.
13. Nadeau NJ, et al. (2014) Population genomics of parallel hybrid zones in the

mimetic butterflies, *H. melpomene* and *H. erato*. *Genome Res* 24(8):1316–1333.
14. Mallet J, Beltrán M, Neukirchen W, Linares M (2007) Natural hybridization in heliconiine butterflies: the species boundary as a continuum. *BMC Evol Biol* 7(1):28.
15. Mazo-Vargas A, et al. (2017) Macroevolutionary shifts of *WntA* function potentiate butterfly wing-pattern diversity. *Proc Natl Acad Sci* 114(40):10701 LP-10706.

Supplemental methods

Butterfly stocks and developmental staging

Butterfly colonies for postman (*Heliconius erato petiverana*), radiate (*Heliconius erato lativitta*), and one derived phenotype (*Heliconius himera*) were initiated and maintained using individuals imported from Ecuador and Costa Rica, kept in greenhouses at approximately 30C, and reared on *Passiflora biflora*, and *Lantana camara* and *Psiguira warscewiczii* flowers as previously described (1, 2). Colony individuals were observed to assess purity of red color patterns prior to performing ATAC-seq, ChIP-seq, and Hi-C assays. *Dryas iulia* samples were obtained from a colony derived from imported individuals from Costa Rica, maintained in greenhouses at 30C and reared on *P. biflora* and *L. camara* flowers. *H. melpomene* samples were taken from individuals imported from Costa Rica and Ecuador.

Developmental staging for butterflies was determined by pupal age (day 3 post-pupation and day 5 post-pupation, *H. erato* and *D. iulia* samples) or by morphological characteristics (ommochrome stage: approximately 7 days post-pupation with red wing patterns deposited and lacking melanin pigmentation, and day 3 post-pupation: wings fully sized with scale buds just beginning to show, *H. erato* and *H. melpomene,* respectively).

Preparation of ATAC-seq, ChIP-seq, and Hi-C libraries

ATAC-seq libraries for *H. melpomene* and *D. iulia* were prepared as previously described with minor modifications to the original protocol (2, 3). In brief, day 3 (*H. melpomene*) and day 5 *(D. iulia*) wings were dissected in cold PBS and homogenized with a dounce homogenizer. Cells were counted using a hemocytometer and lysed with ATAC lysis buffer. The following formula was used to calculate cell number for transposition: 3.2Gb (human genome) divided by the genome size of sample species (e.g. 454Mb for *D. iulia*), multiplied by 50,000. Cells were incubated with Tn5 following the original protocol, amplified for 10-11 cycles, and purified with 1.8x Ampure Beads.

ChIP-seq libraries were prepared using a sonication-based protocol modified from Lewis et al. 2016 (1). Wing tissue was dissected from day 3 (*H. erato*) and day 5 (*D. iulia*, when

optix expression in the wing increases) and fixed for 6 minutes while rocking at room temperature in 1% formaldehyde. Fixation was quenched with glycine, tissues were washed twice with cold PBS and flash frozen on dry ice. Fixed tissue samples were thawed on ice and dounced briefly with a dounce homogenizer. Cells were incubated for 5 minutes on ice in ATAC-seq lysis buffer to lyse cells, spun for 5 minutes at 2000xg in a 4C centrifuge, then resuspended in 150uL ChIP Dilution Buffer. Chromatin was sheared with a Bioruptor, using the settings: 3 x 5 min, 30 sec. on/30 sec. off, setting: high. 500-750uL ChIP Dilution Buffer was added to the sheared samples and samples were centrifuged at 12000xg for 10 minutes at 4C to clear the nuclear prep. 20-50ug sheared chromatin was then used for each immunoprecipitation assay, with ChIP Dilution Buffer added to approximately 1mL volume. 9uL of optix antibody was added to each IP, after which the IP assay was performed following the previous protocol. Library preparation of immunoprecipitated fragments and an input DNA control was performed using the NEBNext DNA Ultra II kit following manufacturer recommendations. No size selection was performed.

Hi-C libraries were made using the protocol of Rao et al. 2013 (4) with some modifications: Wing tissue was fixed and flash frozen following the same protocol as used for ChIP-seq assays. Three sets of forewings or hindwing tissues were used for each Hi-C replicate (approximately 25-35 million cells). Tissue was briefly dounced with a 2mL dounce homogenizer to disrupt tissue and isolate nuclei, followed by a spin at 2000xg for 5 minutes at 4C to pellet nuclei. The pellet was then treated with lysis buffer following the original protocol to lyse any remaining cells. Nuclei were permeabilized using 0.1% SDS for 10 minutes at 62C, and DpnII was used for a 3-4 hour restriction digest at 37C. Following purification of proximity ligated DNA, an additional step was added to remove any unligated biotin as described in (5). Samples were sheared using a Covaris S2 sonicator with the settings: Duty Cycle: 10%, Intensity: 4, Cycles/Burst: 200, Time: 50sec. A size selection of sheared fragments was performed using 1.2x Ampure beads to remove small fragments that were unlikely to produce two useable end sequences. Following the isolation of biotinylated DNA, libraries were prepared with the NEB DNA Ultra II library prep kit. All samples were sequenced at the Cornell University sequencing core facility on a NextSeq 500 (SI Appendix, Table S1).

Analysis of structural variation

optix CRE loci were extracted from the *H. e. lativitta* reference genome along with 2,000 bp flanking regions on either end using the Samtools function, faidx (6). Loci with relatively low distance between them were extracted and analyzed as a single sequence (e.g. LR1+LR2 and U1+U2). Extracted sequences were then aligned to *H. e. demophoon* reference genome with the MUMmer NUCmer tool using default parameters (7). Using genotype calls files from available whole genome re-sequences for 79 H. erato individuals sampled across its range (8), we extracted individual genotypes for the genomic regions containing the optix CREs. Genotypes were filtered and grouped by phenotype (radiate vs. postman) and run with custom R scripts that calculates coverage per basepair (number of individuals with genotype call per site). The resulting plots included (1) the alignment for the *H. e. demophoon* and *H. e. lativitta* reference genomes, (2) genotype

coverage for individuals with different phenotypes and (3) the positions of insertions/deletions that showed associations with red pattern differences. The indels associated with wing pattern variation were shown for sites with 100% differences in coverage (i.e. perfect associations with the indel and color pattern) and for sites with genomes an 80:20 percent difference threshold

Data analysis for ATAC-seq, ChIP-seq, and Hi-C samples

ATAC-seq and ChIP-seq data were processed as previously described: Paired-end reads were aligned to the corresponding reference assembly for each species available at lepbase.org (*H. e. lativitta* version 1, *H. e. demophoon* version 1, *H. melpomene melpomene* version 2, and a draft assembly of *Dryas iulia*) (1, 8, 9) using Bowtie2 (10). A custom script was used to filter for mapping quality of greater than 20 and to remove reads with multiple high-quality alignments. Picardtools "markduplicates" was then used to filter PCR duplicates. Files were read depth normalized and genome browser tracks were generated with the ENCODE script "bedGraphToBigWig". Peaks and variable loci between populations for ATAC-seq and ChIP-seq samples were manually curated around the *optix* locus.

Orthology of ATAC-seq peaks between species was determined using Satsuma2 (11) for synteny analysis. Peaks were classified as wholly conserved if synteny aligned peaks in both species, and were considered functionally conserved (DNA sequence is not alignable, but peak presence appears conserved) if a peak in *H. melpomene* or *D. iulia* was present in a genomic interval with flanking conserved sites between *H. erato* and the other species.

Hi-C libraries were aligned using the Juicer pipeline as described in (12). Virtual 4C plots were generated using a custom python script for a window around *optix* with reads placed into 3kb bins. Interactions between distal enhancer elements and the *optix* promoter were manually curated in a genome browser.

CRISPR mutagenesis and genotyping

CRISPR/Cas9 mutagenesis assays were performed based off of a previously described protocol (13): sgRNAs were generated for sites that tiled across the regulatory loci, matched the N_{20}NGG motif, contained approximately 40-80% GC nucleotides, did not contain an additional G base in the three nucleotides following the NGG PAM sequence, and either blasted uniquely to the reference assembly or showed limited (less than two sites) similarity to other sites with the constraint that potential off target binding could not overlap either an assayed regulatory element or a gene exon (SI Appendix, Table S2). Eggs were collected for approximately 2 hours, after which embryos were injected with a 1:1 ratio of pooled sgRNAs and Cas9 enzyme. sgRNAs for each locus were pooled into groups of 2-4 guide RNAs per injection as shown below (SI Appendix, Table S3). Injected larvae were reared at 28C in incubators and fed *P. biflora*. Adults were screen for mutations using left-right wing comparisons for dorsal and ventral clonal pattern abnormalities.

Select mutants for each regulatory element screened were genotyped for positive CRISPR mutagenesis using PCR (SI Appendix, Table S5). Because lepidopteran wing cells have undergone apoptosis and the DNA is degraded prior to adult emergence, we collected DNA from the head and thorax of mutant individuals for genotyping. PCR primers flanking the expected mutation sites were used to amplify genomic DNA templates followed by gel excision and Sanger sequencing of gel bands at the expected fragment size as well as any bands that differed from wild-type samples. The TIDE software package (14) was then used to confirm mutagenesis efficiency and to verify mutation around expected cut sites compared with wild type individuals.

Phylogenetic analysis

Whole genome 100 bp paired-end Illumina resequencing data of 109 *H. erato* individuals from 16 populations with distinct color patterns was obtained from Van Belleghem et al. 2017 and 2018 (8, 15) and aligned to the *H. e. lativitta* reference genome using BWA v0.7.13 (16) with default parameters. From the aligned reads, genotypes were called using the Genome Analysis Tool Kit (GATK) Haplotypecaller (17) with default parameters and the genotypes were filtered for minimum depth ≥ 10 and genotype quality (GQ) ≥ 30. Genotypes were next extracted for CREs and phylogenetic relationships among individuals were inferred for these intervals using maximum likelihood (ML) trees with RAxML v8.0.26 (18). The best likelihood tree was chosen from 100 trees generated from a distinct starting tree using a GTR model with CAT approximation of rate heterogeneity and the support values of this tree were Inferred with 100 bootstrap replicates. Phylogentic weighting analysis used to refine the predicted regulatory intervals for *optix* was performed as previously described (8) using alignments against the *H. e. lativitta* genome assembly.

Coalescence analysis

ARGweaver (19) is a tool for estimating local genealogies from whole genome sequencing data, based on a discrete-time model of coalescence and recombination (20). We ran ARGweaver on the VCF file containing 109 genomes, masking out regions of the genome with repeats > 300nt. We used an unpublished feature (available at https://github.com/CshlSiepelLab/argweaver) that can parse genotype probabilities from the PL field of the VCF file, and takes these probabilities into account rather than using absolute genotype calls. We also used the --unphased option, which does not require phased samples and instead integrates over genotype phase. ARGweaver was run for 2000 iterations independently for two regions: Hel_chr18_1:40000-230000, and Hel_chr18_1:700000-800000. We used a mutation rate of 2.9e-9/bp/generation, a recombination rate of 5.5e-8/bp/generation, and a diploid population size of 2e6. The discrete time points of the ARGweaver model were distributed on a logarithmic time scale, with a maximum coalescence time of 2e8 generations. The trees produced in this paper we taken from the final iteration of the ARGweaver anaysis, and colored by population.

References for supplemental methods

1. Lewis JJ, van der Burg KRL, Mazo-Vargas A, Reed RD (2016) ChIP-seq-annotated *Heliconius erato* genome highlights patterns of cis-regulatory evolution in Lepidoptera. *Cell Rep* 16(11):2855–2863.
2. Lewis JJ, Reed RD (2018) Genome-wide regulatory adaptation shapes population-level genomic landscapes in *Heliconius*. *Mol Biol Evol*. doi:10.1093/molbev/msy209.
3. Buenrostro JD, Giresi PG, Zaba LC, Chang HY, Greenleaf WJ (2013) Transposition of native chromatin for fast and sensitive epigenomic profiling of open chromatin, DNA-binding proteins and nucleosome position. *Nat Methods* 10(12):1213–1218.
4. Rao SSP, et al. (2014) A 3D map of the human genome at kilobase resolution reveals principles of chromatin looping. *Cell* 159(7):1665–80.
5. Belaghzal H, Dekker J, Gibcus JH (2017) Hi-C 2.0: An optimized Hi-C procedure for high-resolution genome-wide mapping of chromosome conformation. *Methods* 123:56–65.
6. Li H, et al. (2009) The Sequence Alignment/Map format and SAMtools. *Bioinformatics* 25(16):2078–2079.
7. Marçais G, et al. (2018) MUMmer4: A fast and versatile genome alignment system. *PLOS Comput Biol* 14(1):e1005944.
8. Van Belleghem SM, et al. (2017) Complex modular architecture around a simple toolkit of wing pattern genes. *Nat Ecol Evol* 1(3):0052.
9. Davey JW, et al. (2016) Major improvements to the *Heliconius melpomene* genome assembly used to confirm 10 chromosome fusion events in 6 million years of butterfly evolution. *G3 (Bethesda)* 6(3):695–708.
10. Langmead B, Salzberg SL (2012) Fast gapped-read alignment with Bowtie 2. *Nat Methods* 9(4):357–9.
11. Grabherr MG, et al. (2010) Genome-wide synteny through highly sensitive sequence alignment: Satsuma. *Bioinformatics* 26(9):1145–51.
12. Durand NC, et al. (2016) Juicer provides a one-click system for analyzing loop-resolution Hi-C experiments. *Cell Syst* 3(1):95–8.
13. Zhang L, Reed RD (2016) Genome editing in butterflies reveals that *spalt* promotes and *Distal-less* represses eyespot colour patterns. *Nat Commun* 7(1):11769.
14. Brinkman EK, Chen T, Amendola M, van Steensel B (2014) Easy quantitative assessment of genome editing by sequence trace decomposition. *Nucleic Acids Res* 42(22):e168.
15. Van Belleghem SM, et al. (2018) Patterns of Z chromosome divergence among *Heliconius* species highlight the importance of historical demography. *Mol Ecol* 27(19):3852–3872.
16. Li H, Durbin R (2010) Fast and accurate long-read alignment with Burrows–Wheeler transform. *Bioinformatics* 26(5):589–595.
17. Van der Auwera GA, et al. (2013) From FastQ data to high-confidence variant calls: The genome analysis toolkit best practices pipeline. *Current Protocols in Bioinformatics* (John Wiley & Sons, Inc., Hoboken, NJ, USA), p 11.10.1-11.10.33.
18. Stamatakis A (2014) RAxML version 8: a tool for phylogenetic analysis and post-

analysis of large phylogenies. *Bioinformatics* 30(9):1312–1313.
19. Rasmussen MD, Hubisz MJ, Gronau I, Siepel A (2014) Genome-wide inference of ancestral recombination graphs. *PLoS Genet* 10(5):e1004342.
20. McVean GAT, Cardin NJ (2005) Approximating the coalescent with recombination. *Philos Trans R Soc B Biol Sci* 360(1459):1387–1393.

Supplemental Figures

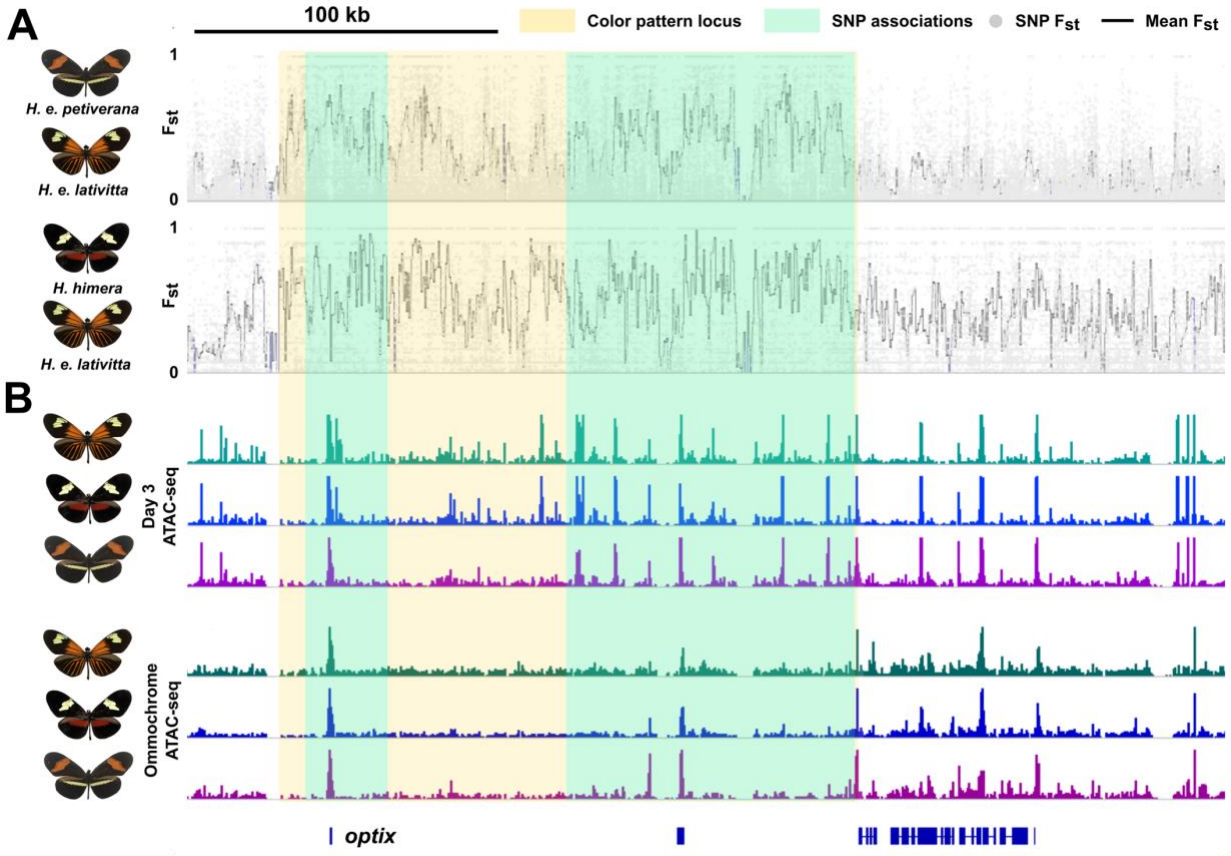

Figure S1. SNP differentiation and ATAC-seq profiles for *H. erato* populations. (A) Plots showing SNP Fst between races used in this study. Yellow shading highlights the broad mendelian locus associated with red wing pattern variation. Green shading shows general regions of SNP associations with red wing pattern variation. **(B)** ATAC-seq tracks for *H. e. petiverana, H. e. lativitta*, and *H. himera* (from top to bottom) for both developmental stages used in this study.

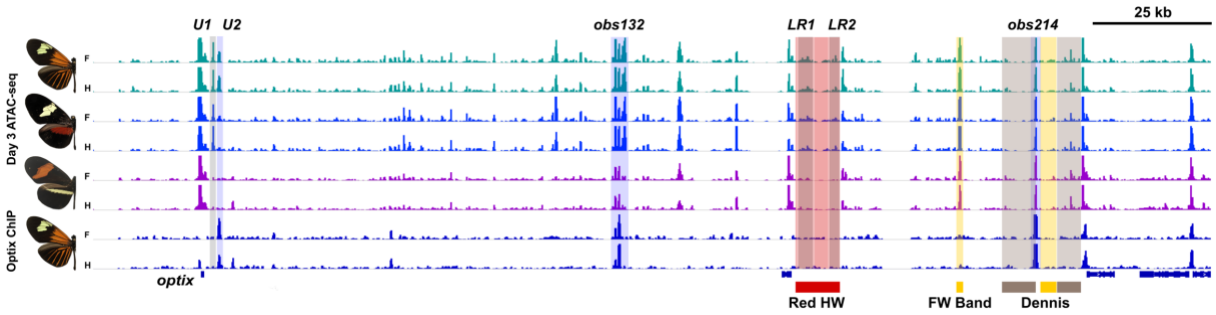

Figure S2. Loci associated with red wing pattern variation within and between species using phylogenetic weighting. ATAC-seq tracks showing *optix* CREs with loci associated with red wing pattern variation highlighted. Red shading indicates phylogenetic weights associated with variation in the presence or absence of red patterns on the hindwing between species. Yellow shading marks loci associated with variation in distal red forewing red patterns between species and gray marks loci associated with the presence or absence of the dennis element in French Guiana.

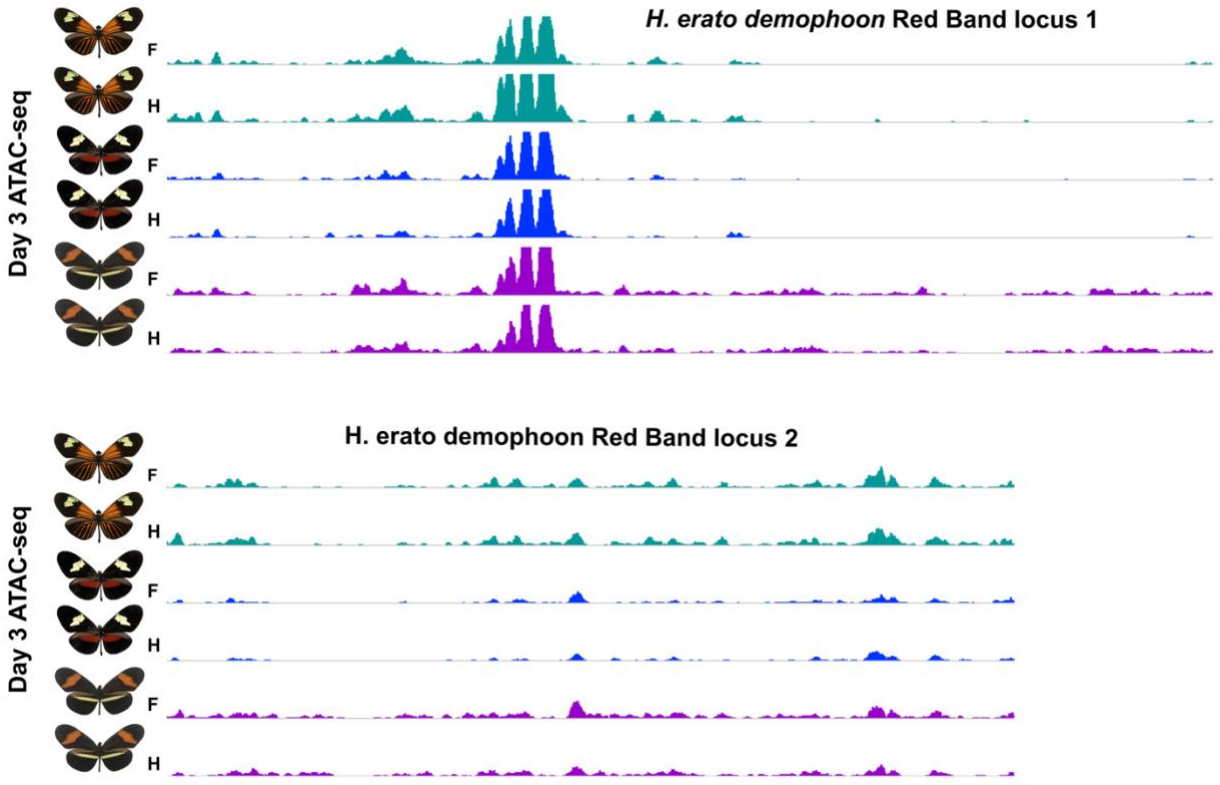

Figure S3. ATAC-seq profiles at predicted loci associated with postman red color pattern. ATAC-seq tracks for *H. e. lativitta*, *H. himera*, and *H. e. petiverana* (from top to bottom) show no significant variation in accessibility over SNP association interval linked with the postman red forewing phenotype. Alignments of ATAC-seq data were done on the *H. e. demophoon* postman genome assembly.

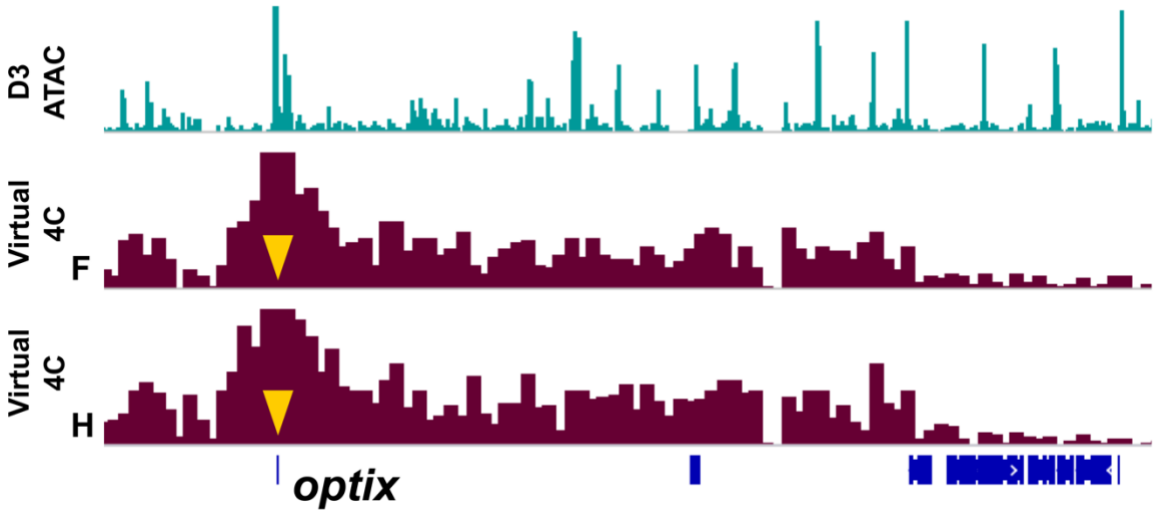

Figure S4. Virtual 4C tracks at the *optix* promoter in forewing and hindwing tissue. Virtual 4C tracks show similar enrichment profile around *optix* in forewing and hindwing datasets.

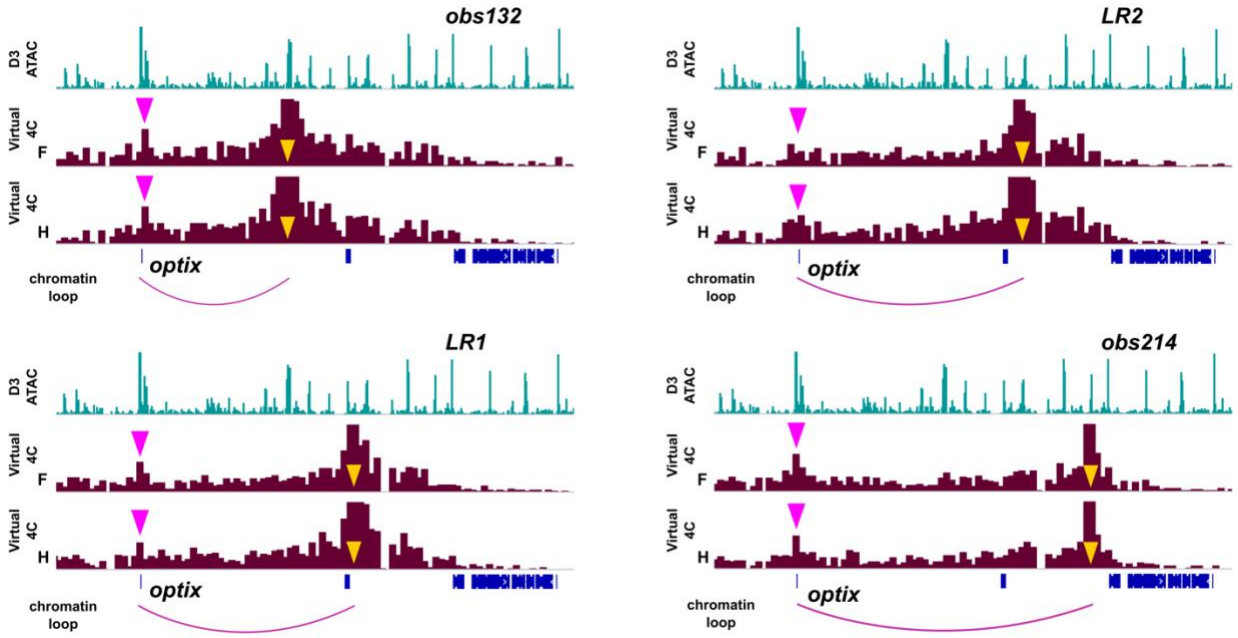

Figure S5. Forewing and hindwing virtual 4C tracks for *obs132*, *LR1*, *LR2*, and *obs214*. Virtual 4C tracks show similar enrichment profiles for enhancer loci *obs132*, *LR1*, *LR2*, and *obs214* in forewing and hindwing datasets.

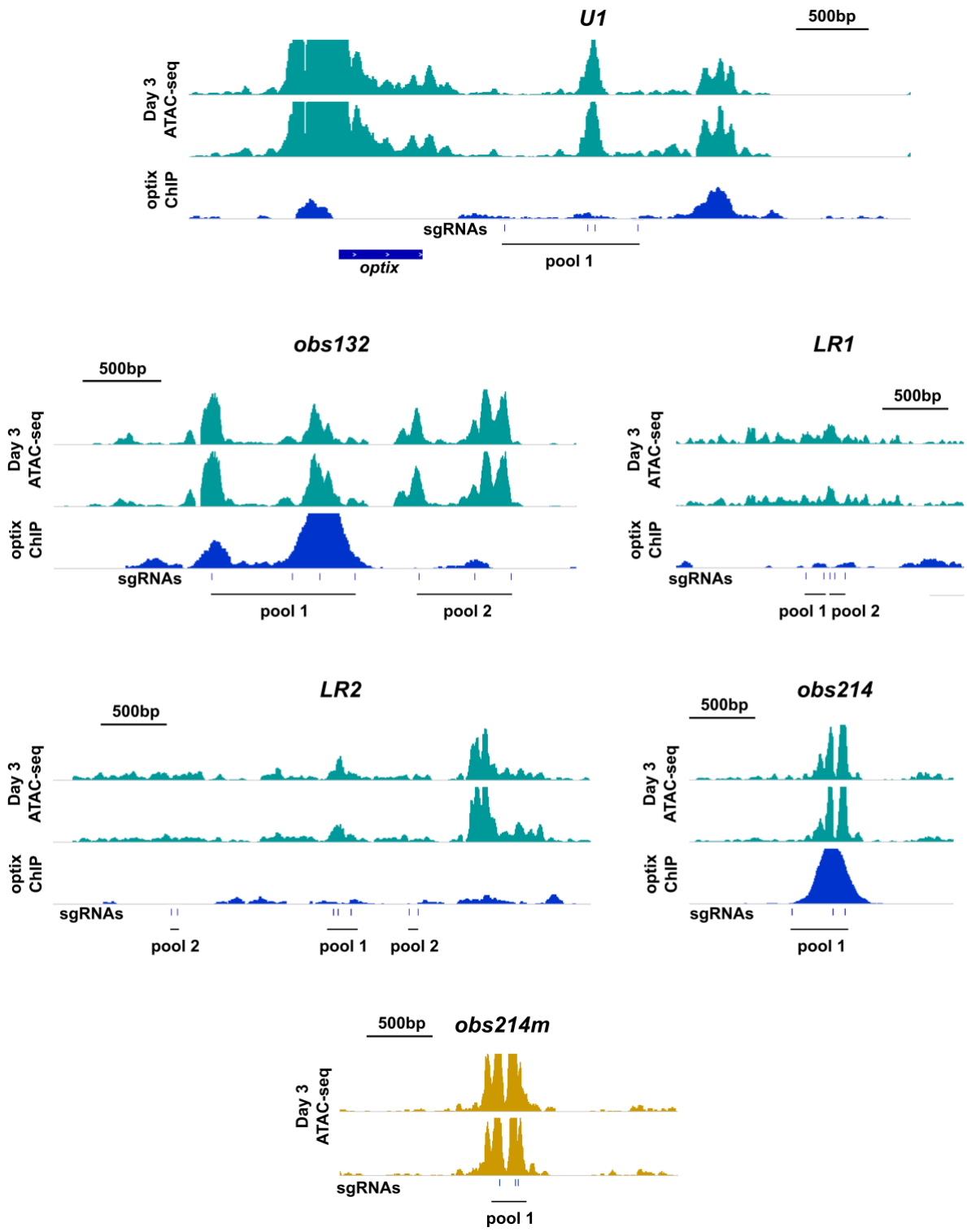

Figure S6. Location of sgRNAs used for CRISPR mutagenesis of enhancer loci. Visual representation of sgRNA locations relative to ATAC-seq peaks for each of the five regulatory loci screened using CRISPR.

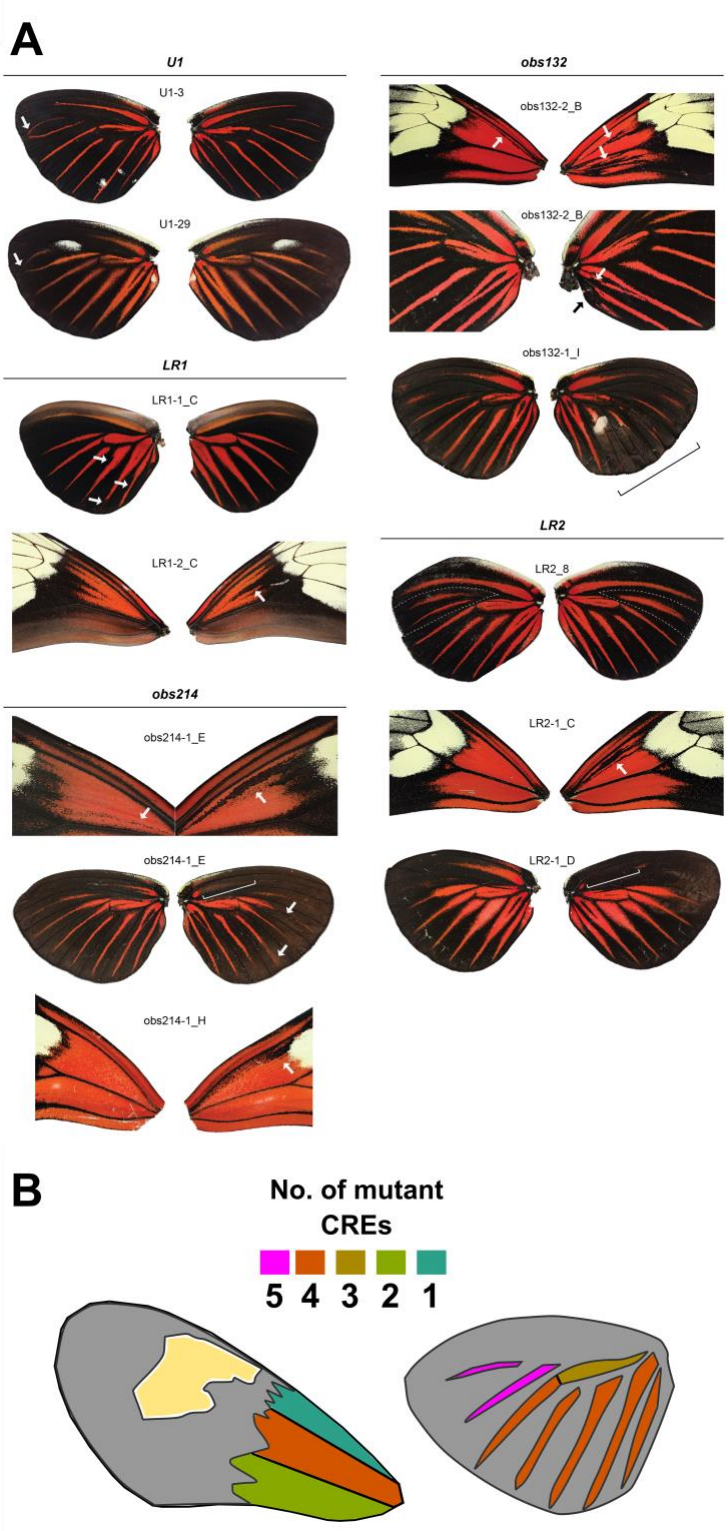

Figure S7. Additional examples of mosaic deletion mutants for *U1*, *obs132*, *LR1*, *LR2*, and *obs214*. (A) Phenotypic effects of mosaic CRE deletions are annotated by arrows and/or dashed lines. A full summary of deletion mutants is presented in Table S4. **(B)** Diagram showing number of CRE mutants by wing section (forewing) or ray (hindwing).

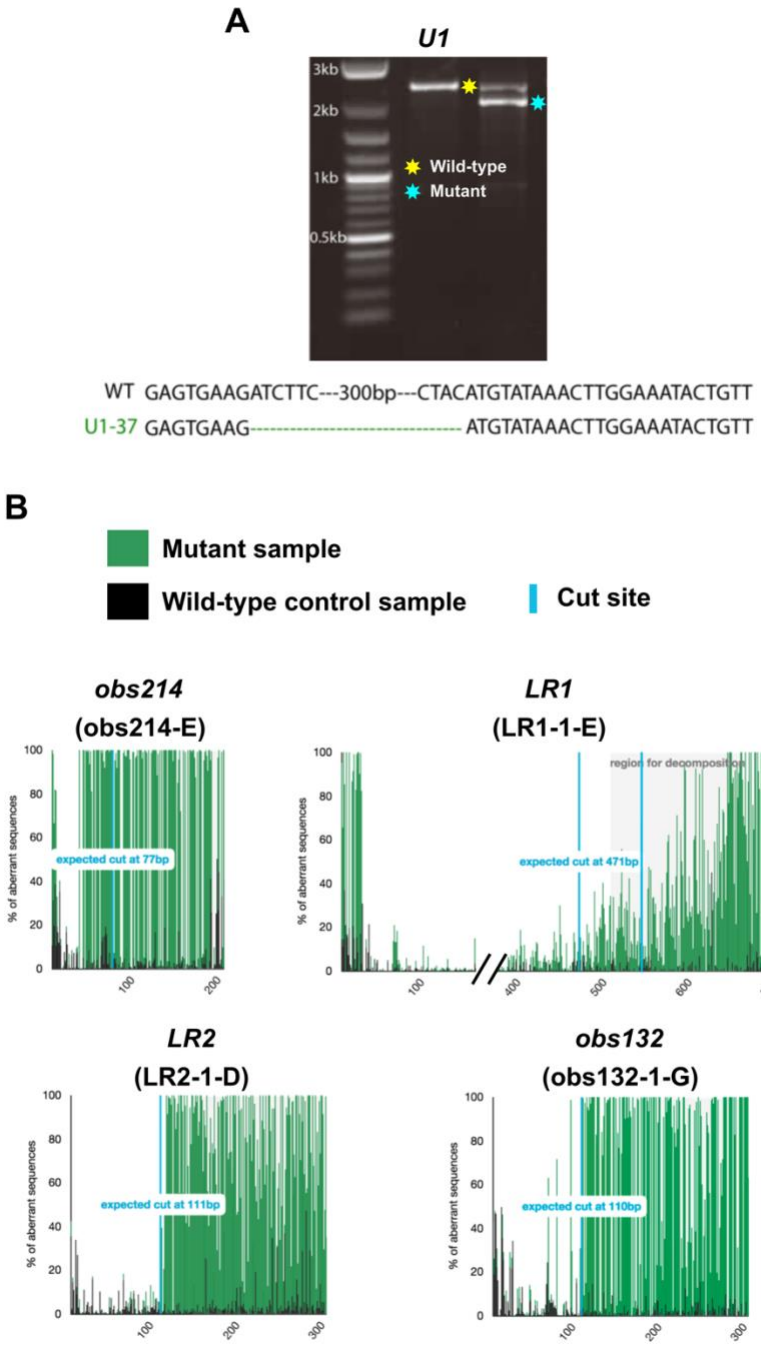

Figure S8. Examples of genotyping results for CRISPR mutants for *U1*, *obs132*, *LR1*, *LR2*, and *obs214* enhancer loci. (**A**) PCR for *U1* mutant sample U1-37 showing alternate gel band. Sequence of gel band with 300bp absent relative to wild-type shown below. (**B**) TIDE analysis for four samples showing aberrant mutation profiles around expected cut sites for *obs214*, *LR1*, *LR2*, and *obs132*. Sample names shown in parentheses.

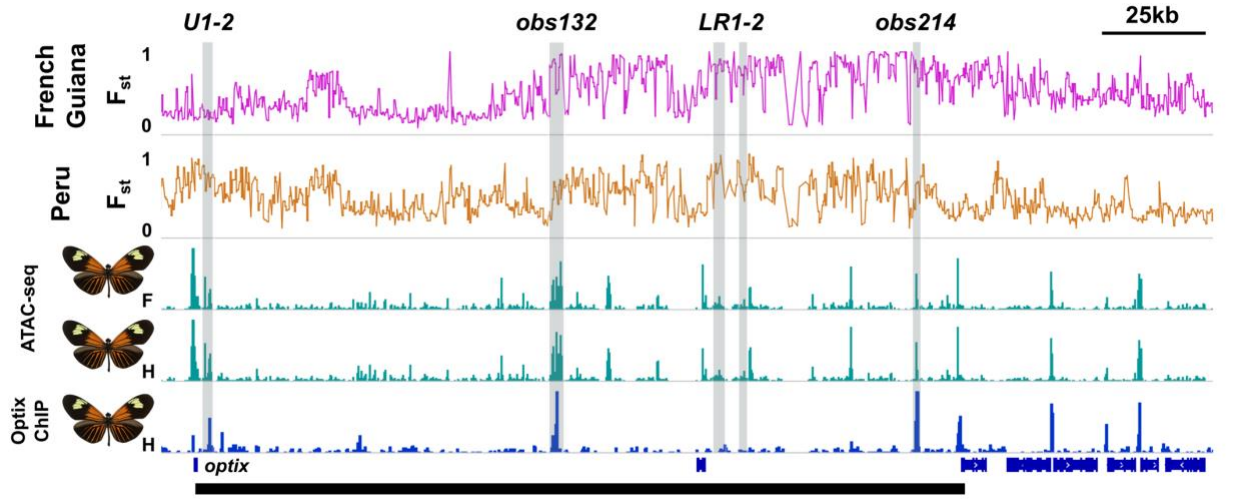

Figure S9. Examples of genomic differentiation at hybrid zones. Fst tracks show some variation in F_{st} along the *optix* locus for hybrid zones between morphs in French Guiana and Peru. Black bar shows region used to calculate the local background F_{st} value used in Figure 4.

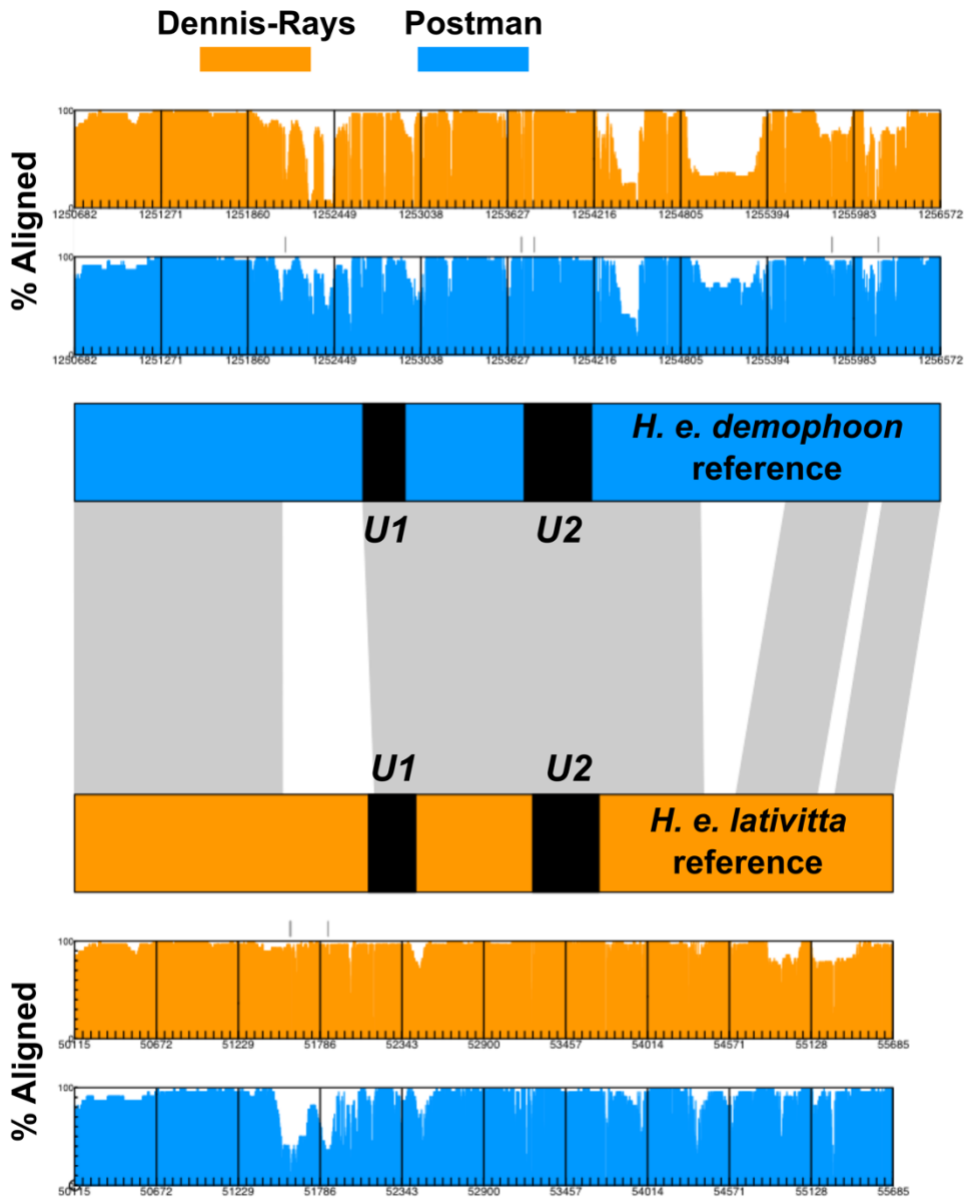

Figure S10. Structural sequence variation between postman and radiate for *U1* and *U2*. Alignments of *U1* and *U2* loci between *de novo* genome assemblies for radiate assembly *H. e. lativitta* (orange) and postman assembly *H. e. demophoon* (blue). Middle bars show CREs (black) and assembly synteny (gray shading between bars). Tracks above show DNA sequence alignment percent against the *H. e. demophoon* assembly from all postman (blue) and radiate (orange) samples. Gray bars above sequence alignment tracks show indels with at least 80% conservation by phenotype, black bars indicate 100% conservation of indels by phenotype. Tracks below show the same using the *H. e. lativitta* assembly.

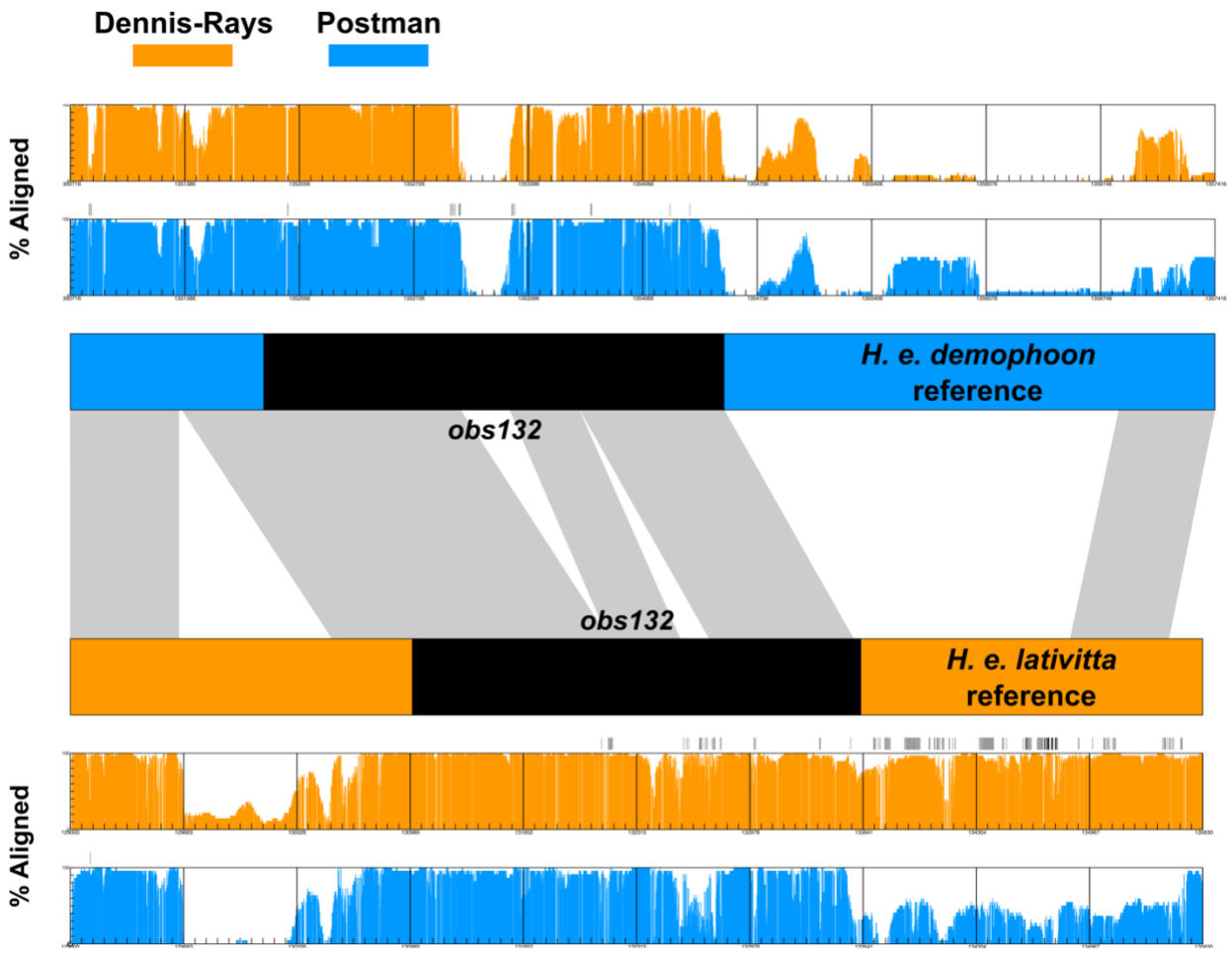

Figure S11. Structural sequence variation between postman and radiate for *obs132*. Alignments of the *obs132* locus between *de novo* genome assemblies for radiate assembly *H. e. lativitta* (orange) and postman assembly *H. e. demophoon* (blue). Middle bars show CREs (black) and assembly synteny (gray shading between bars). Tracks above show DNA sequence alignment percent against the *H. e. demophoon* assembly from all postman (blue) and radiate (orange) samples. Gray bars above sequence alignment tracks show indels with at least 80% conservation by phenotype, black bars indicate 100% conservation of indels by phenotype. Tracks below show the same using the *H. e. lativitta* assembly.

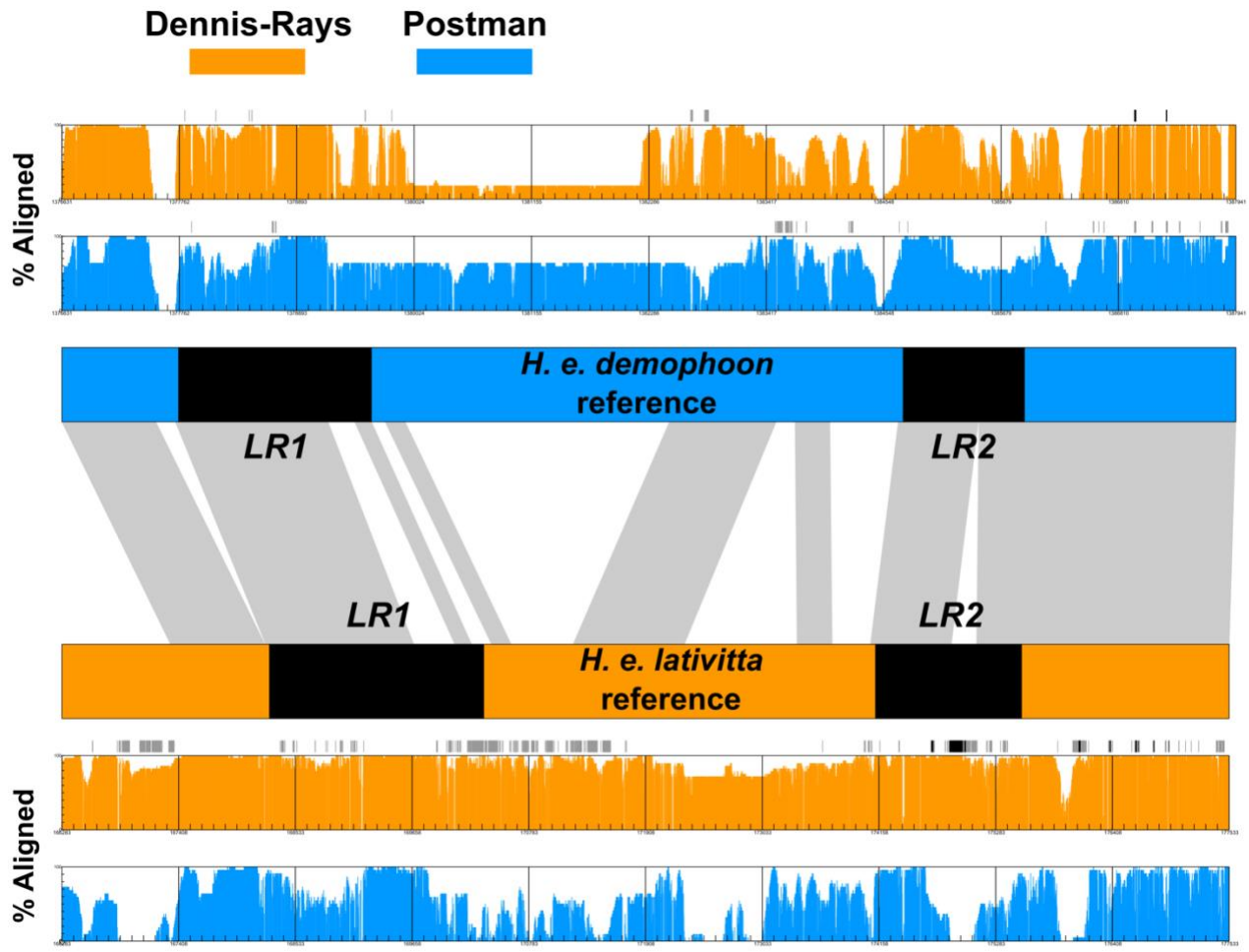

Figure S12. Structural sequence variation between postman and radiate for *LR1* and *LR2*. Alignments of *LR1* and *LR2* loci between *de novo* genome assemblies for radiate assembly *H. e. lativitta* (orange) and postman assembly *H. e. demophoon* (blue). Middle bars show CREs (black) and assembly synteny (gray shading between bars). Tracks above show DNA sequence alignment percent against the *H. e. demophoon* assembly from all postman (blue) and radiate (orange) samples. Gray bars above sequence alignment tracks show indels with at least 80% conservation by phenotype, black bars indicate 100% conservation of indels by phenotype. Tracks below show the same using the *H. e. lativitta* assembly.

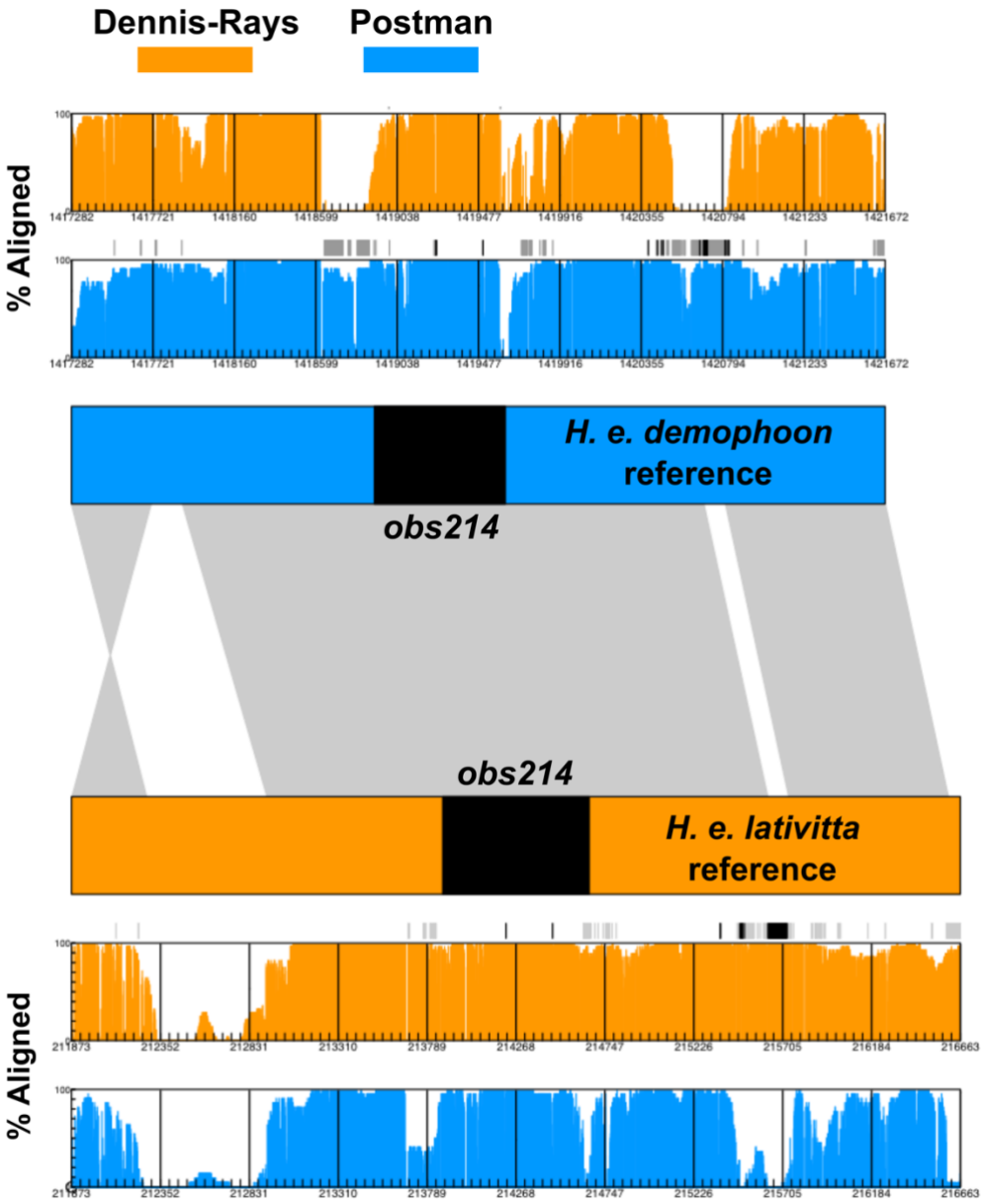

Figure S13. Structural sequence variation between postman and radiate for *obs214*. Alignment of the *obs214* locus between *de novo* genome assemblies for radiate assembly *H. e. lativitta* (orange) and postman assembly *H. e. demophoon* (blue). Middle bars show the CREs (black) and assembly synteny (gray shading between bars). Tracks above show DNA sequence alignment percent against the *H. e. demophoon* assembly from all postman (blue) and radiate (orange) samples. Gray bars above sequence alignment tracks show indels with at least 80% conservation by phenotype, black bars indicate 100% conservation of indels by phenotype. Tracks below show the same using the *H. e. lativitta* assembly.

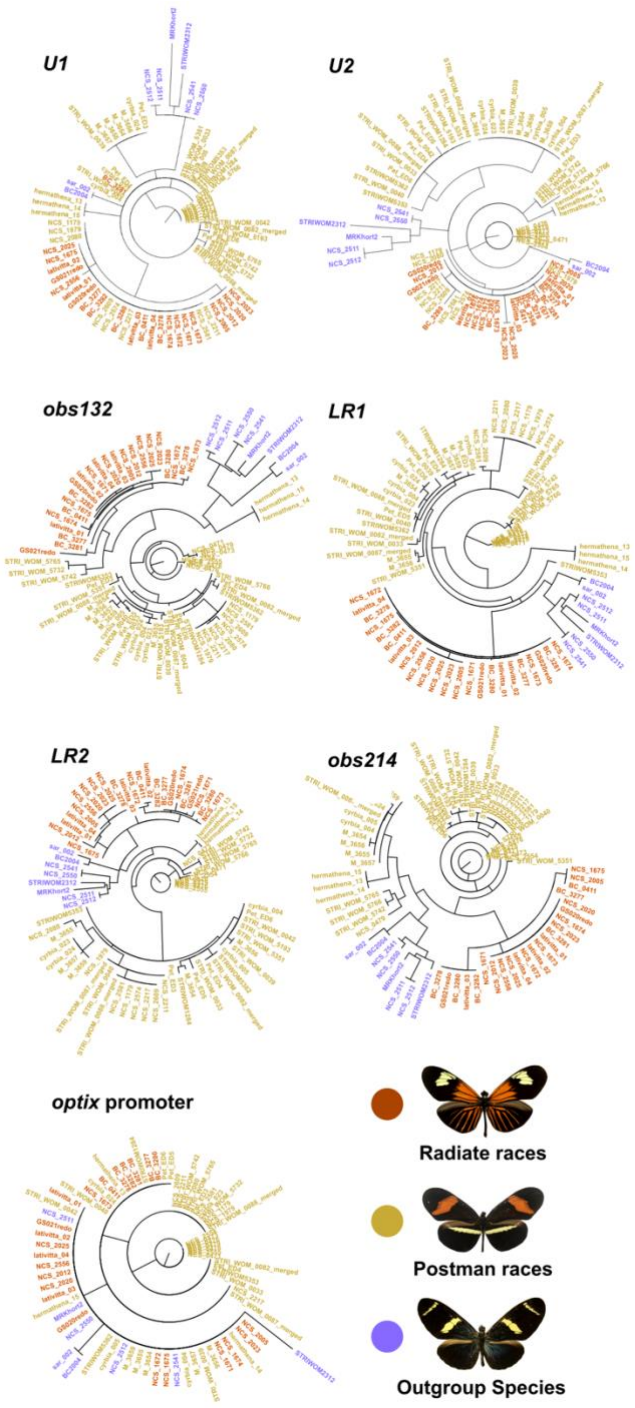

Figure S14. Maximum likelihood phylogenies for *optix* CREs in *H. erato* with sample IDs. Maximum likelihood phylogeny for only radiate and postman morphs along with outgroup species. Trees are colored by phenotype, with radiate (orange), postman (yellow) and outgroups (purple). Postman morphs placed with the radiate group are from *H. e. hydara* in French Guiana. *H. e. hydara* morphs from Panama are placed with the remainder of the postman races.

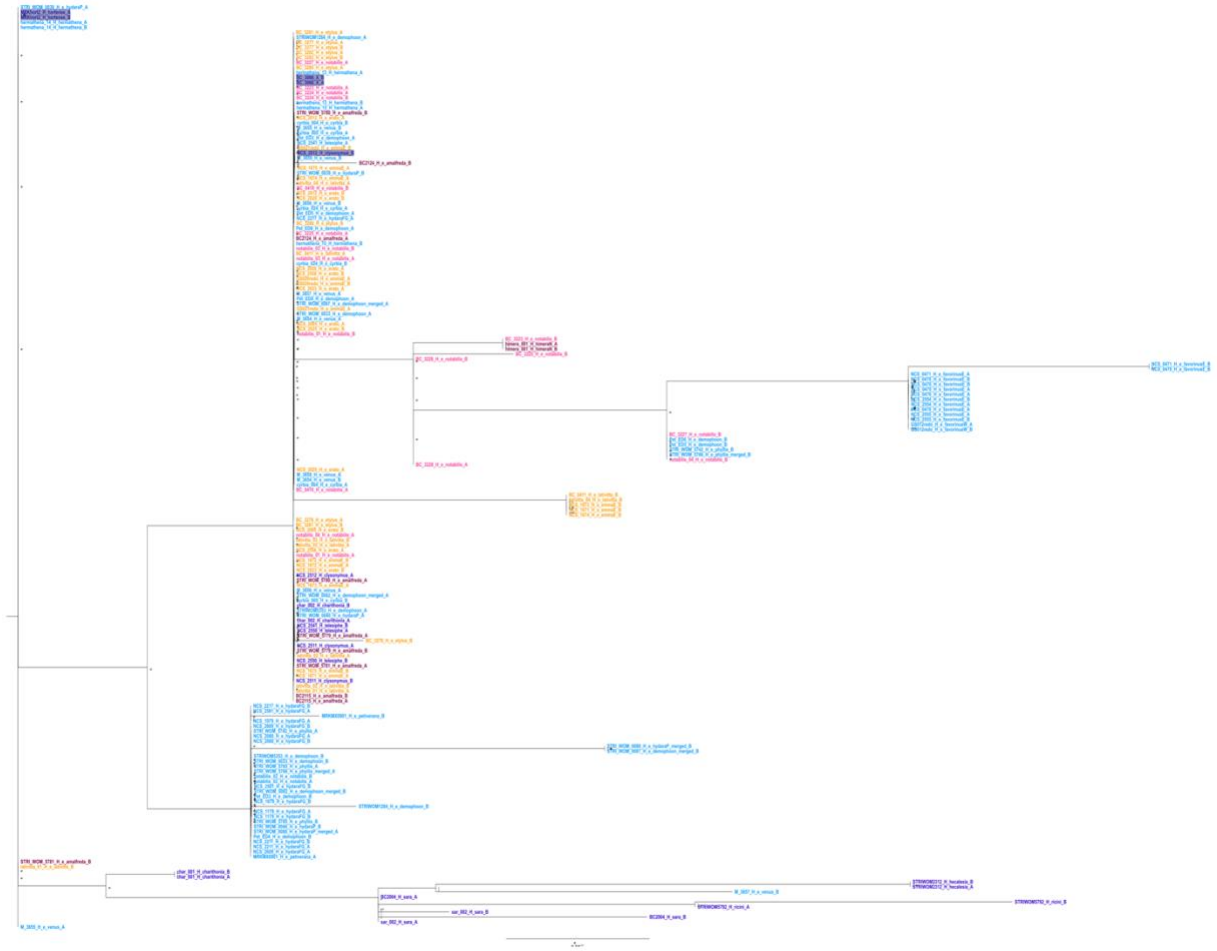

Figure S15. Maximum likelihood phylogeny for the *optix* promoter in *H. erato*. Maximum likelihood phylogeny colored by phenotype including all morphs, with radiate (orange), postman (blue), outgroups (purple), derived Amazon morphs (maroon), and derived *H. e. notabilis* morph (pink).

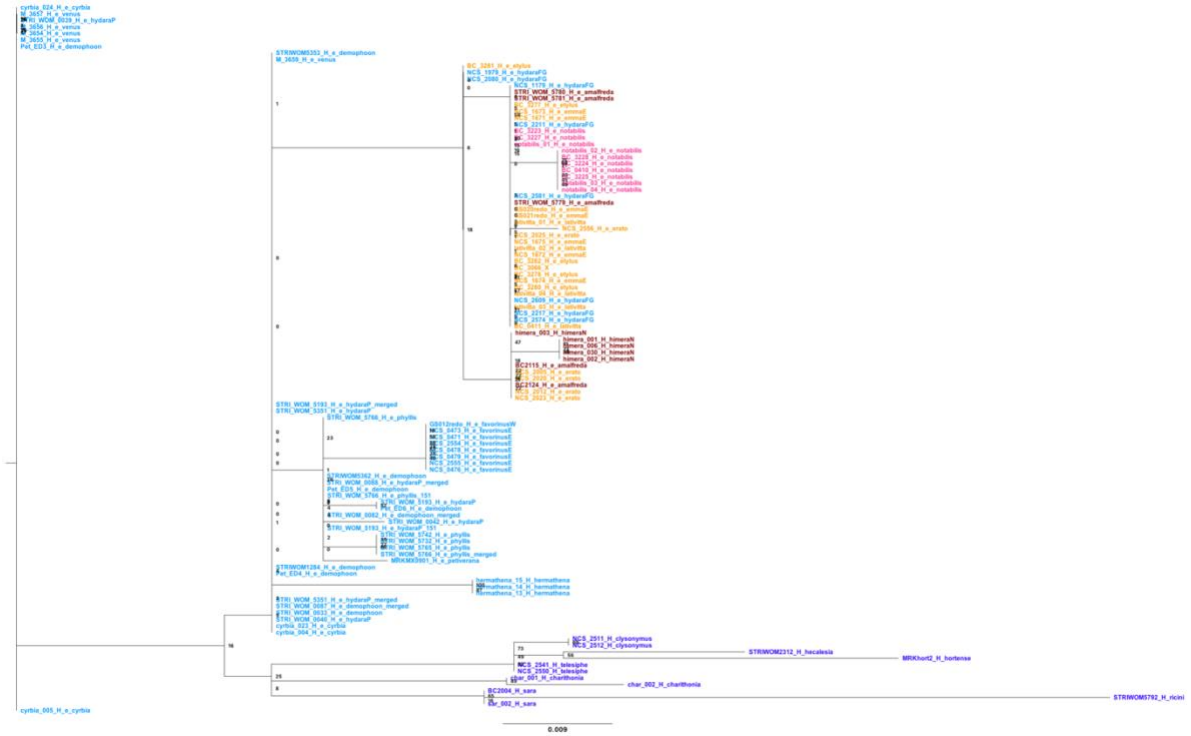

Figure S16. Maximum likelihood phylogeny for *U1* in *H. erato*. Maximum likelihood phylogeny colored by phenotype including all morphs, with radiate (orange), postman (blue), outgroups (purple), derived Amazon morphs (maroon), and derived *H. e. notabilis* morph (pink).

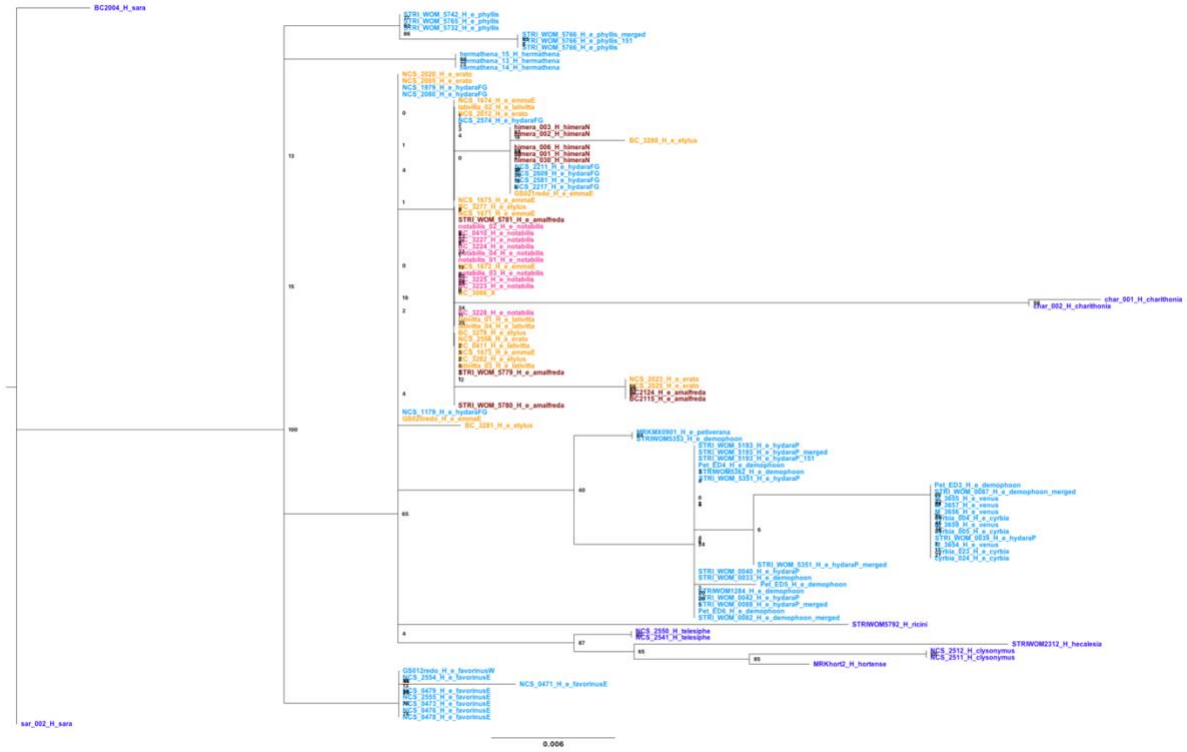

Figure S17. Maximum likelihood phylogeny for *U2* in *H. erato*. Maximum likelihood phylogeny colored by phenotype including all morphs, with radiate (orange), postman (blue), outgroups (purple), derived Amazon morphs (maroon), and derived *H. e. notabilis* morph (pink).

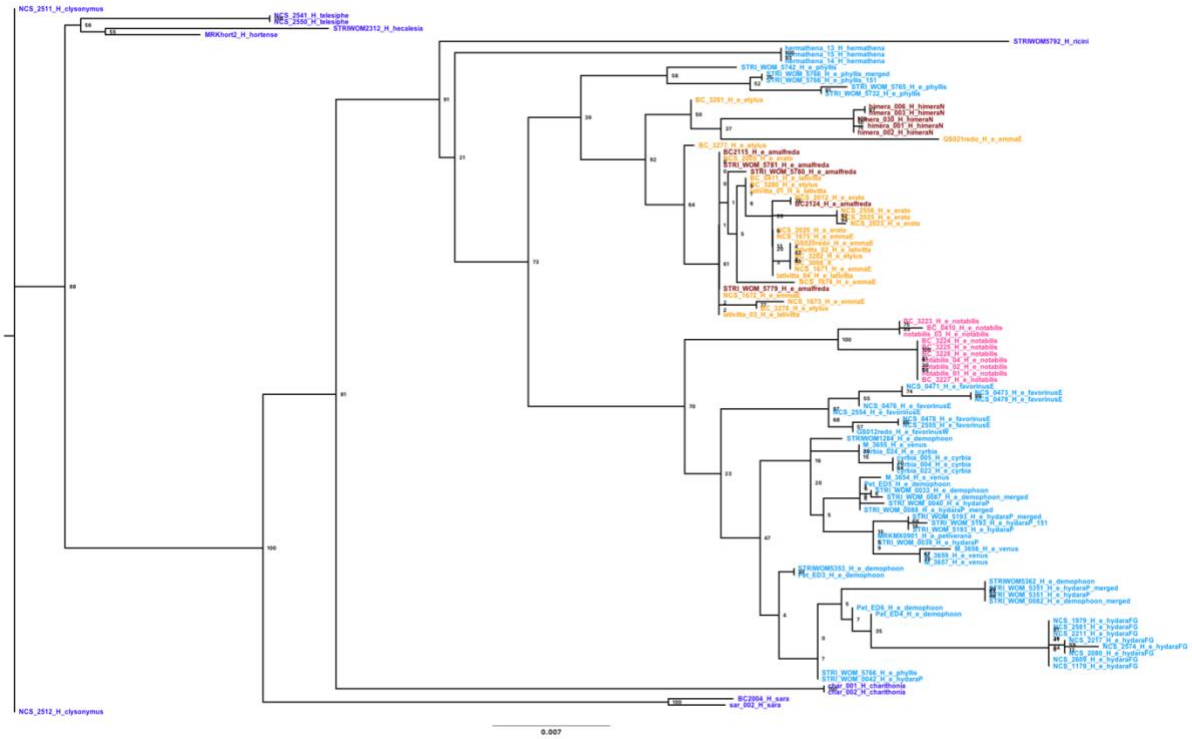

Figure S18. Maximum likelihood phylogeny for *obs132* in *H. erato*. Maximum likelihood phylogeny colored by phenotype including all morphs, with radiate (orange), postman (blue), outgroups (purple), derived Amazon morphs (maroon), and derived *H. e. notabilis* morph (pink).

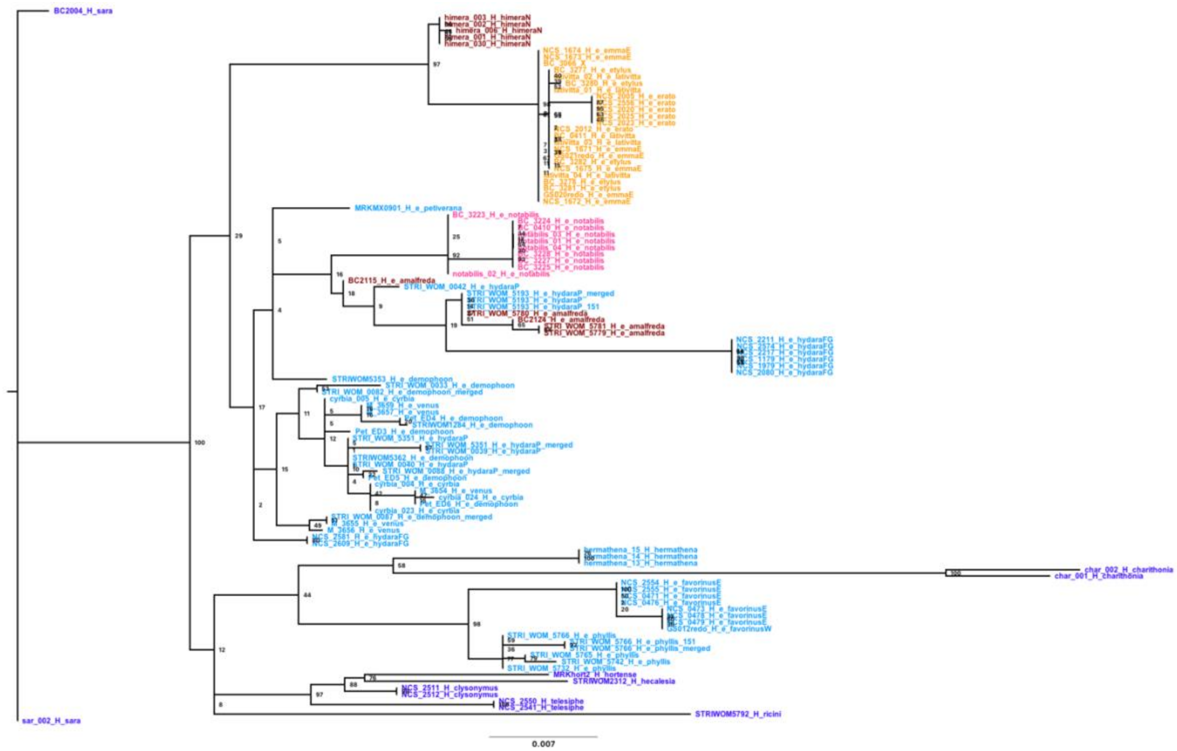

Figure S19. Maximum likelihood phylogeny for *LR1* in *H. erato*. Maximum likelihood phylogeny colored by phenotype including all morphs, with radiate (orange), postman (blue), outgroups (purple), derived Amazon morphs (maroon), and derived *H. e. notabilis* morph (pink).

Figure S20. Maximum likelihood phylogeny for *LR2* in *H. erato*. Maximum likelihood phylogeny colored by phenotype including all morphs, with radiate (orange), postman (blue), outgroups (purple), derived Amazon morphs (maroon), and derived *H. e. notabilis* morph (pink). The single postman allele embedded in the radiate clade is likely derived from a heterozygous individual.

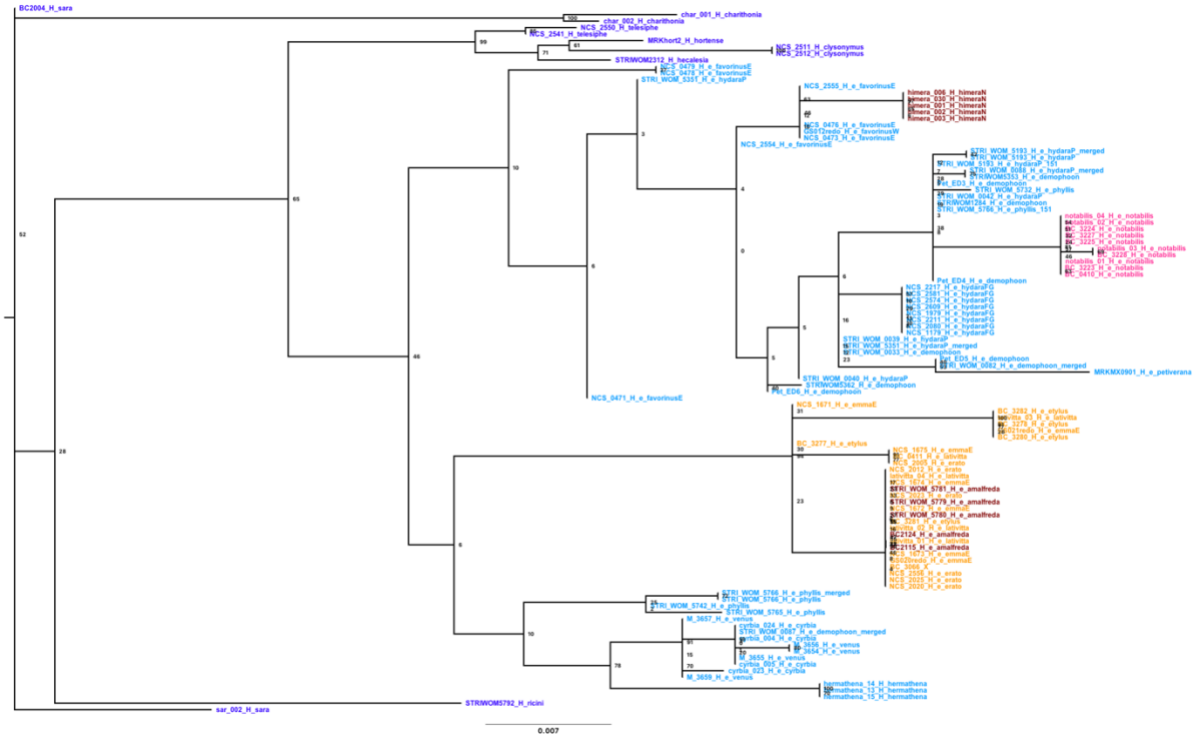

Figure S21. Maximum likelihood phylogeny for *obs214* in *H. erato*. Maximum likelihood phylogeny colored by phenotype including all morphs, with radiate (orange), postman (blue), outgroups (purple), derived Amazon morphs (maroon), and derived *H. e. notabilis* morph (pink).

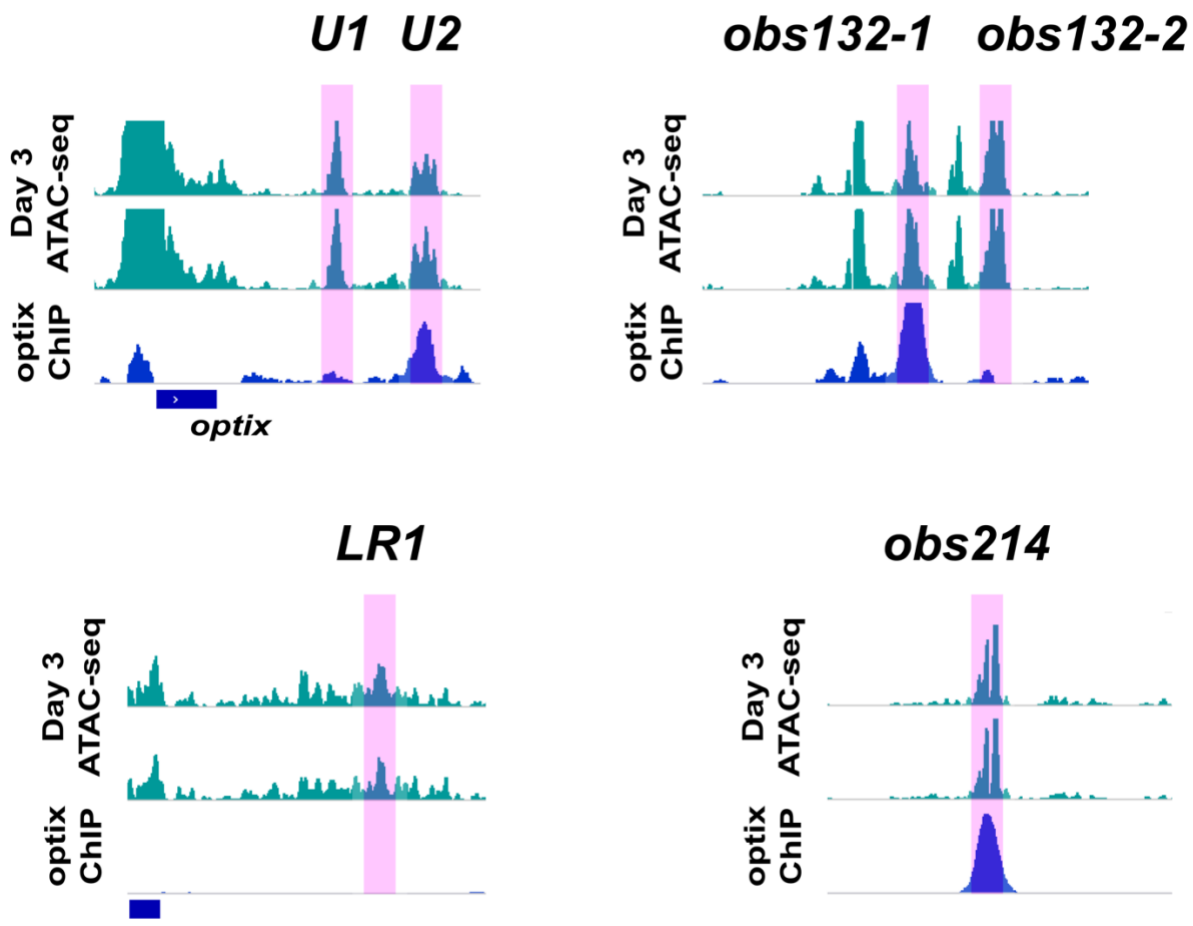

Figure S22. Loci used for coalescence analysis of *optix* CREs. Browser tracks showing the loci (highlighted pink) used to produce coalescence trees in ARGweaver. Two trees were produced for *obs132*, corresponding to the largest peaks with and without optix binding.

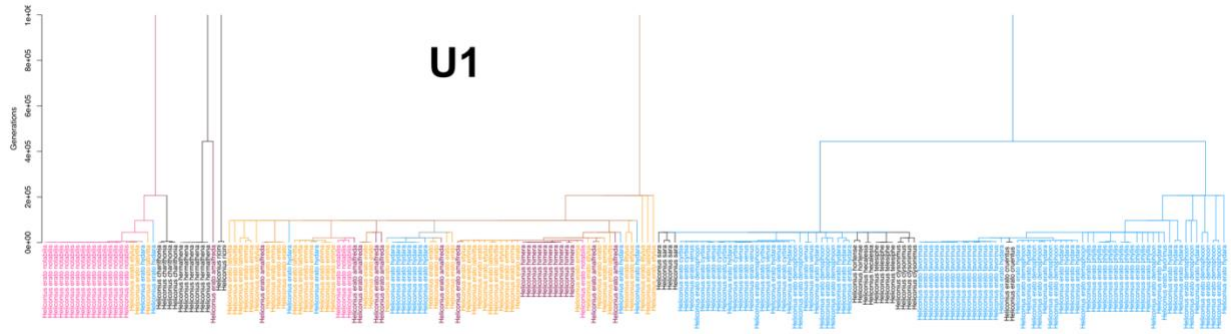

Figure S23. Coalescence tree for *U1* in *H. erato*. Coalescence tree from ARGweaver colored by phenotype, with radiate (orange), postman (blue), outgroups (black), derived Amazon morphs (maroon), and derived *H. e. notabilis* morph (pink).

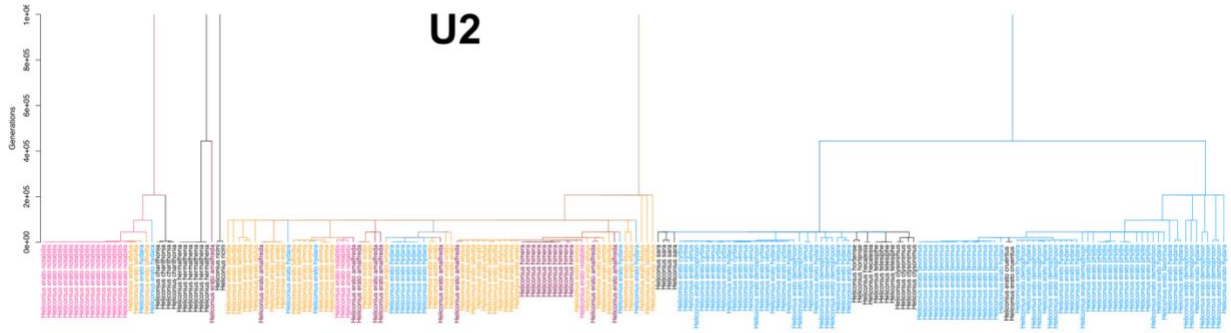

Figure S24. Coalescence tree for *U2* in *H. erato*. Coalescence tree from ARGweaver colored by phenotype, with radiate (orange), postman (blue), outgroups (black), derived Amazon morphs (maroon), and derived *H. e. notabilis* morph (pink).

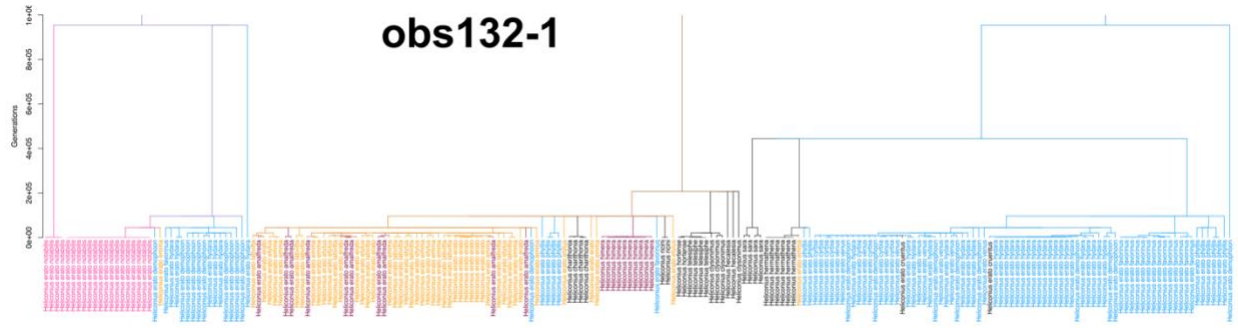

Figure S25. Coalescence tree for *obs132-1* in *H. erato*. Coalescence tree from ARGweaver colored by phenotype, with radiate (orange), postman (blue), outgroups (black), derived Amazon morphs (maroon), and derived *H. e. notabilis* morph (pink).

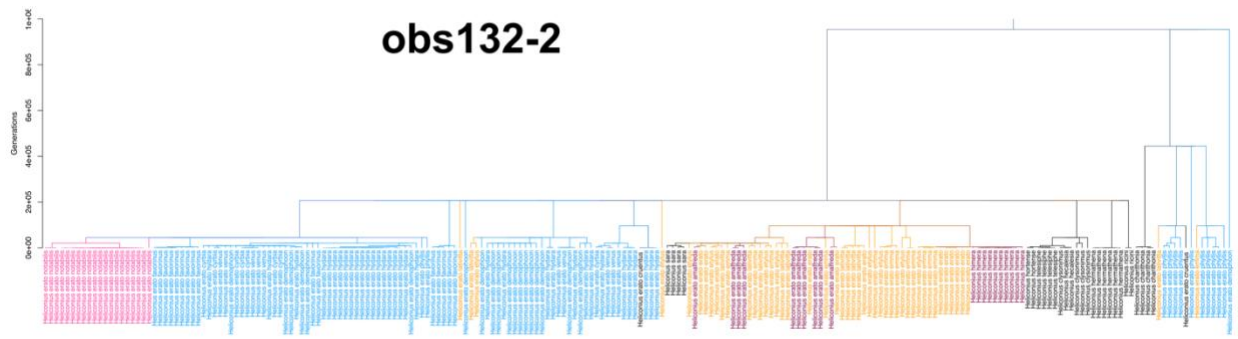

Figure S26. Coalescence tree for *obs132-2* in *H. erato*. Coalescence tree from ARGweaver colored by phenotype, with radiate (orange), postman (blue), outgroups (black), derived Amazon morphs (maroon), and derived *H. e. notabilis* morph (pink).

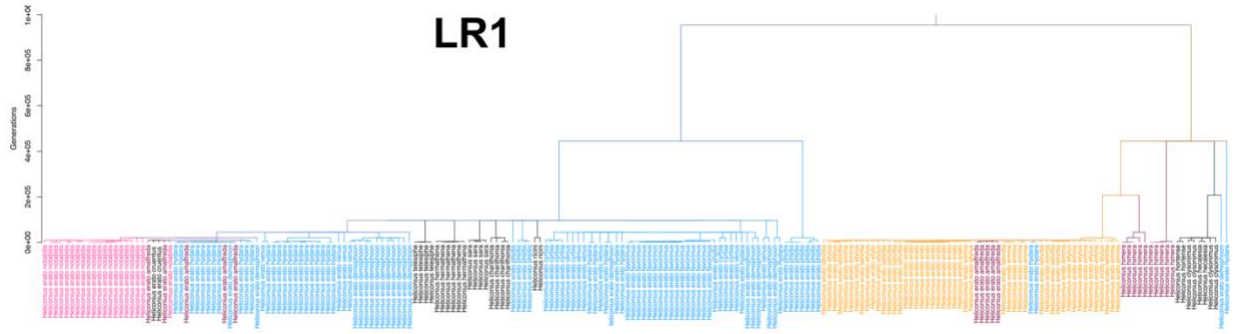

Figure S27. Coalescence tree for *LR1* in *H. erato*. Coalescence tree from ARGweaver colored by phenotype, with radiate (orange), postman (blue), outgroups (black), derived Amazon morphs (maroon), and derived *H. e. notabilis* morph (pink).

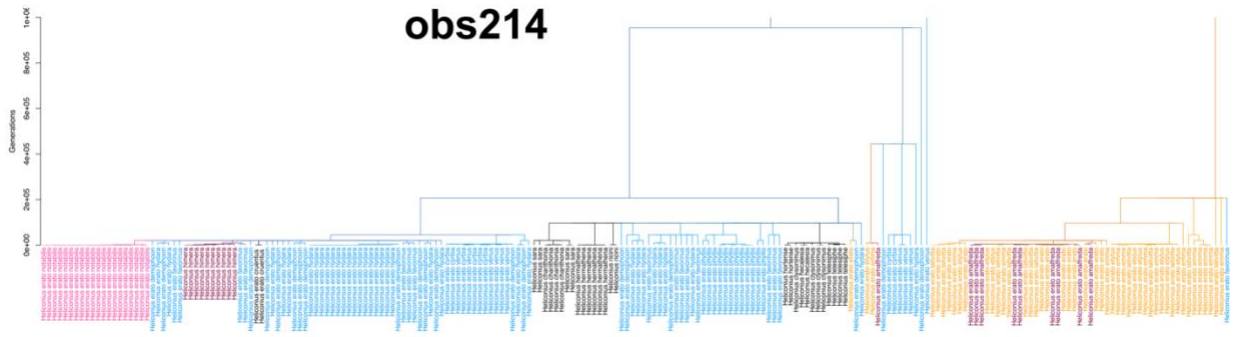

Figure S28. Coalescence tree for *obs214* in *H. erato*. Coalescence tree from ARGweaver colored by phenotype, with radiate (orange), postman (blue), outgroups (black), derived Amazon morphs (maroon), and derived *H. e. notabilis* morph (pink).

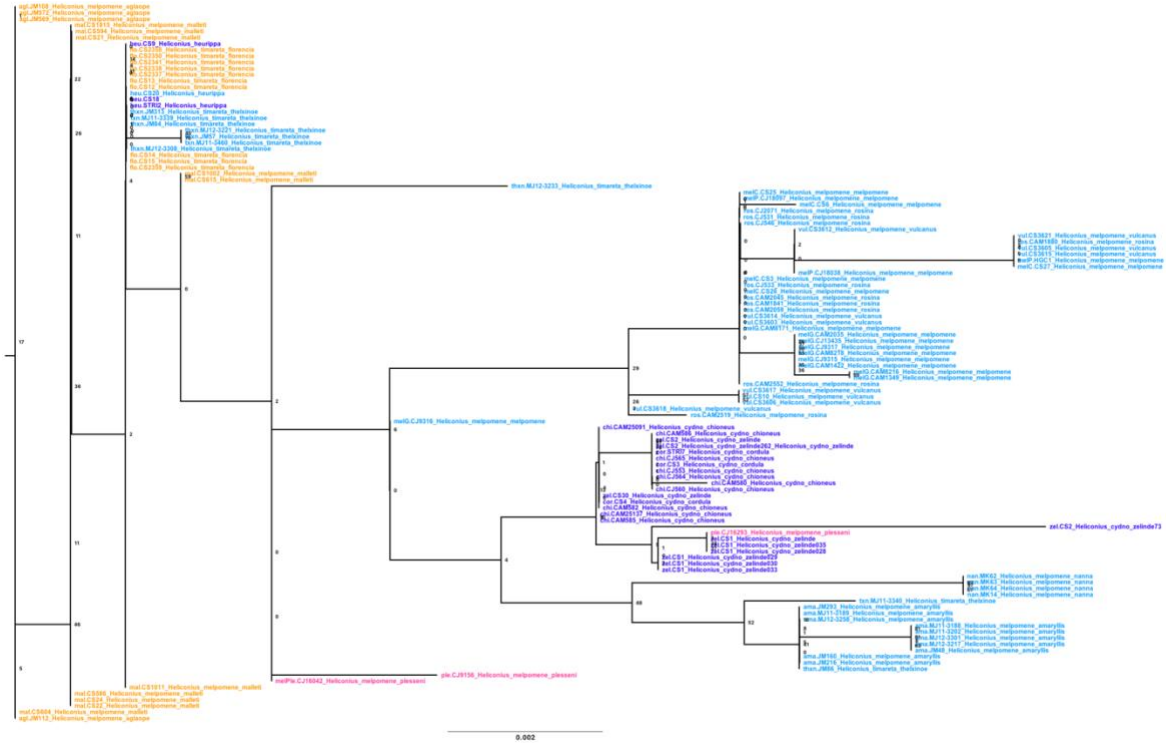

Figure S29. Maximum likelihood phylogeny for the *optix* promoter in *H. melpomene*. Maximum likelihood phylogeny colored by phenotype, with radiate (orange), postman (blue), *H. cydno* group (purple), and *H. m. plesseni* (co-mimic to *H. e. notabilis*) in pink.

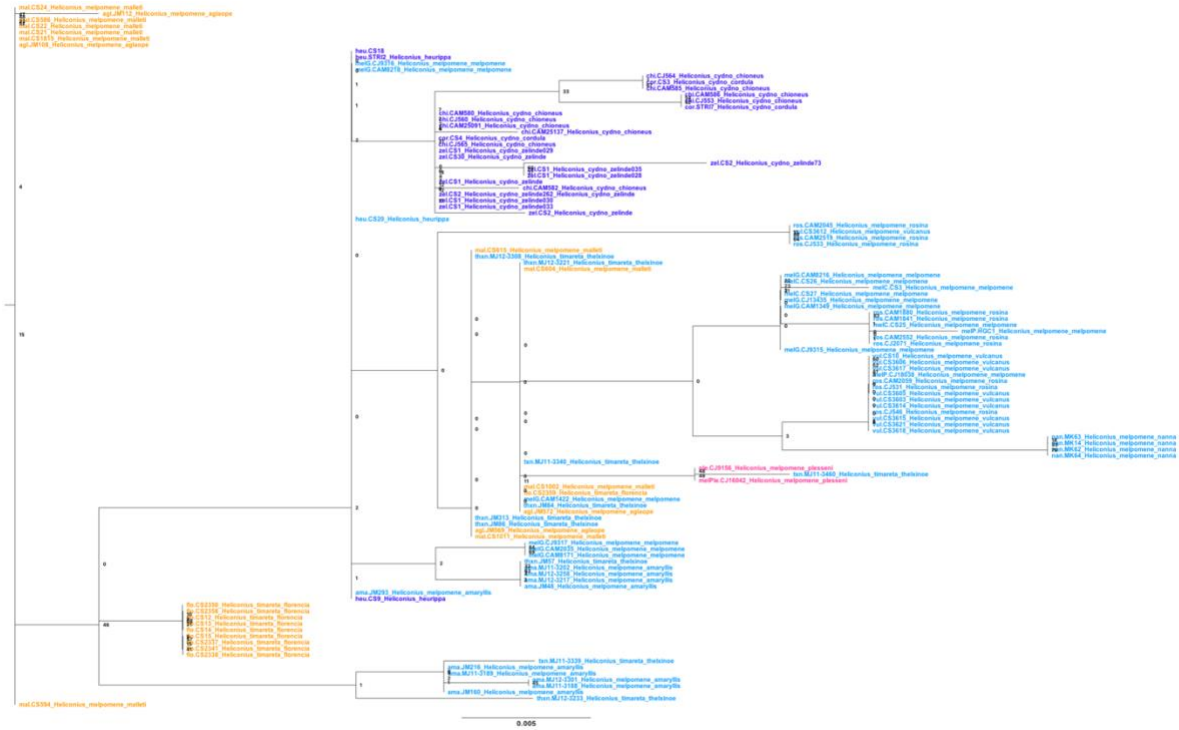

Figure S30. Maximum likelihood phylogeny for *U1* in *H. melpomene*. Maximum likelihood phylogeny colored by phenotype, with radiate (orange), postman (blue), *H. cydno* group (purple), and *H. m. plesseni* (co-mimic to *H. e. notabilis*) in pink.

Figure S31. Maximum likelihood phylogeny for *U2* in *H. melpomene*. Maximum likelihood phylogeny colored by phenotype, with radiate (orange), postman (blue), *H. cydno* group (purple), and *H. m. plesseni* (co-mimic to *H. e. notabilis*) in pink.

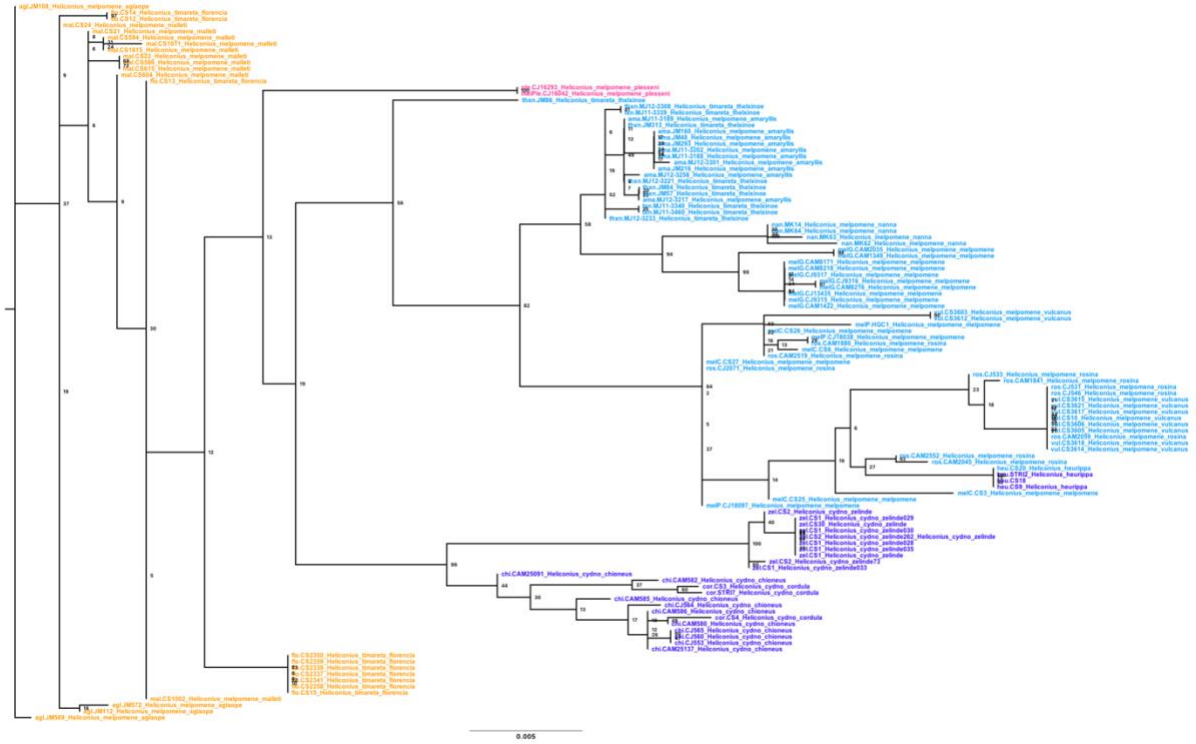

Figure S32. Maximum-liklihood phylogeny for *obs132* in *H. melpomene*. Maximum likelihood phylogeny colored by phenotype, with radiate (orange), postman (blue), *H. cydno* group (purple), and *H. m. plesseni* (co-mimic to *H. e. notabilis*) in pink.

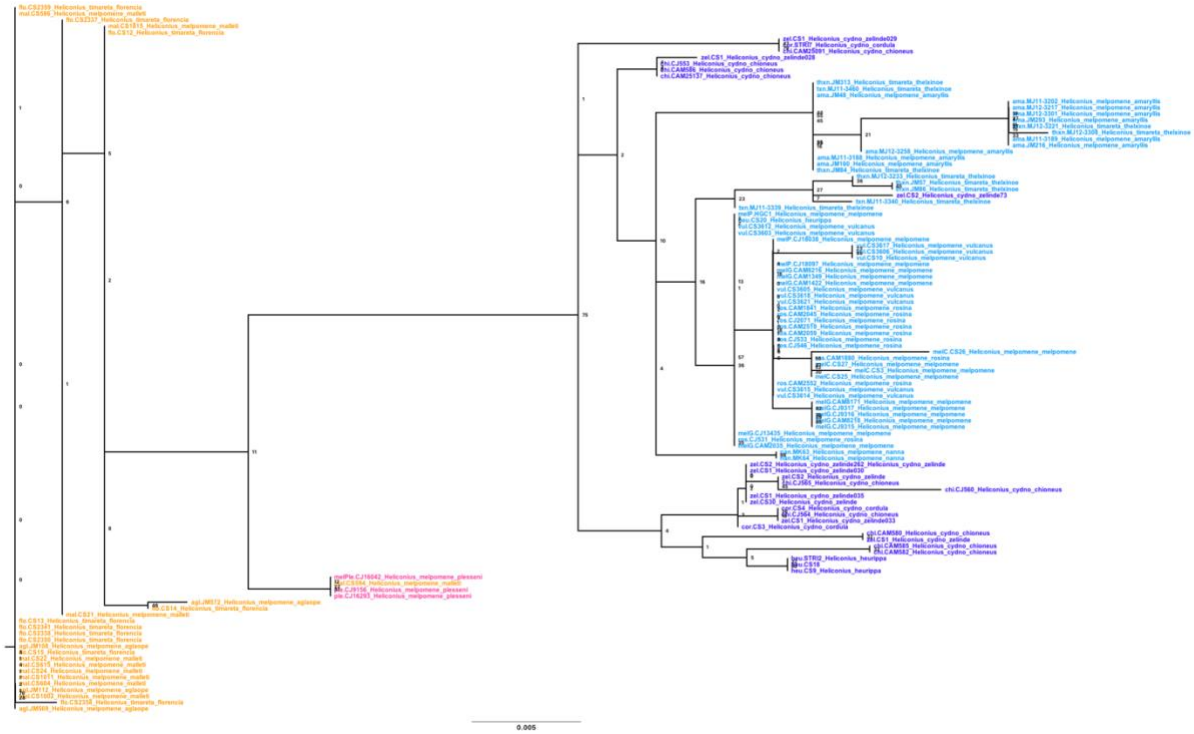

Figure S33. Maximum likelihood phylogeny for *obs214* in *H. melpomene*. Maximum likelihood phylogeny colored by phenotype, with radiate (orange), postman (blue), *H. cydno* group (purple), and *H. m. plesseni* (co-mimic to *H. e. notabilis*) in pink.

Supplemental Tables

Table S1. Genomic data sets sequencing depth and alignment rates.

ATAC-seq

Sample Name	Species	Sequencing Depth (PE reads)	% aligned	post-filter	% post-filter
1-HelatD3-FW-ATAC*	*Heliconius erato lativitta*	74,439,003	78.33	21,291,054	28.60
1-HelatD3-HW-ATAC*	*Heliconius erato lativitta*	92,969,103	79.38	31,106,950	33.46
2-HelatD3-FW-ATAC*	*Heliconius erato lativitta*	78,776,231	81.48	23,532,363	29.87
2-HelatD3-HW-ATAC*	*Heliconius erato lativitta*	71,120,756	81.79	20,696,385	29.10
1-HehimD3-FW-ATAC*	*Heliconius himera*	39,354,840	82.02	14,818,522	37.65
1-HehimD3-HW-ATAC*	*Heliconius himera*	33,000,766	80.04	12,422,448	37.64
2-HehimD3-FW-ATAC*	*Heliconius himera*	29,988,739	68.17	9,010,890	30.05
2-HehimD3-HW-ATAC*	*Heliconius himera*	29,349,657	67.93	8,857,407	30.18
1-HepetD3-FW-ATAC*	*Heliconius erato petiverana*	75,253,026	75.59	19,673,396	26.14
1-HepetD3-HW-ATAC*	*Heliconius erato petiverana*	67,594,090	75.15	17,616,022	26.06
2-HepetD3-FW-ATAC*	*Heliconius erato petiverana*	34,080,006	58.98	8,651,964	25.39
2-HepetD3-HW-ATAC*	*Heliconius erato petiverana*	35,522,496	59.51	9,012,961	25.37
1-HelatOM-FW-ATAC*	*Heliconius erato lativitta*	61,180,678	84.22	17,830,964	29.14
1-HelatOM-HW-ATAC*	*Heliconius erato lativitta*	46,355,229	83.86	14,073,755	30.36
2-HelatOM-FW-ATAC*	*Heliconius erato lativitta*	48,794,391	84.43	13,704,044	28.09
2-HelatOM-HW-ATAC*	*Heliconius erato lativitta*	40,623,963	83.68	11,630,743	28.63
1-HehimOM-FW-ATAC*	*Heliconius himera*	140,258,591	84.51	43,185,833	30.79
1-HehimOM-HW-ATAC*	*Heliconius himera*	108,086,788	84.30	33,224,614	30.74
2-HehimOM-FW-ATAC*	*Heliconius himera*	157,998,378	85.05	46,733,960	29.58
2-HehimOM-HW-ATAC*	*Heliconius himera*	142,928,323	84.15	43,628,546	30.52
1-HepetOM-FW-ATAC*	*Heliconius erato petiverana*	36,147,853	81.72	10,049,169	27.80
1-HepetOM-HW-ATAC*	*Heliconius erato petiverana*	27,114,273	80.90	8,036,949	29.64
2-HepetOM-FW-ATAC*	*Heliconius erato petiverana*	41,149,566	82.58	10,488,852	25.49
2-HepetOM-HW-ATAC*	*Heliconius erato petiverana*	35,523,205	80.37	11,186,877	31.49
ATAC-Hmel_agl_FW-1	*Heliconius melpomene aglaope*	31,317,345	76.73	15,070,114	48.12
ATAC-Hmel_agl_HW-1	*Heliconius melpomene aglaope*	28,448,976	78.83	15,642,390	54.98
ATAC-Hmel_agl_FW-2	*Heliconius melpomene aglaope*	26,200,235	77.26	13,765,775	52.54
ATAC-Hmel_agl_HW-2	*Heliconius melpomene aglaope*	24,846,752	74.32	12,993,777	52.3
ATAC-Hmel_ros_FW-1	*Heliconus melpomene rosina*	31,792,620	83.69	18,190,699	57.22
ATAC-Hmel_ros_HW-1	*Heliconus melpomene rosina*	21,722,841	83.58	12,758,362	58.73
ATAC-Hmel_ros_FW-2	*Heliconus melpomene rosina*	9,455,467	86.15	6,230,986	65.9
ATAC-Hmel_ros_HW-2	*Heliconus melpomene rosina*	16,981,362	85.12	10,620,251	62.54
ATAC-Diulia_mod_FW-1	*Dryas iulia moderata*	52,190,784	89.54	24,620,693	47.17
ATAC-Diulia_mod_FW-2	*Dryas iulia moderata*	46,499,666	88.67	22,705,792	48.83

ChIP-seq

Sample Name	Species	Sequencing Depth (PE reads)	% aligned	post-filter	% post-filter
ChIP_optix_Hera_lat_FW-1	*Heliconius erato lativitta*	9,393,935	77.98	3,324,915	35.39
ChIP_input_Hera_lat_FW-1	*Heliconius erato lativitta*	61,358,108	83.59	21,664,189	35.31
ChIP_optix_Hera_lat_HW-1	*Heliconius erato lativitta*	14,745,471	76.48	5,087,117	34.50
ChIP_input_Hera_lat_HW-1	*Heliconius erato lativitta*	70,528,104	83.54	24,673,980	34.98
ChIP_optix_Hera_lat_FW-2	*Heliconius erato lativitta*	82,045,646	76.84	26,259,379	32.01
ChIP_input_Hera_lat_FW-2	*Heliconius erato lativitta*	104,416,566	85.39	35,365,968	33.87
ChIP_optix_Hera_lat_HW-2	*Heliconius erato lativitta*	54,731,805	82.66	17,849,417	32.61
ChIP_input_Hera_lat_HW-2	*Heliconius erato lativitta*	131,756,998	85.41	44,737,741	33.95
ChIP_optix_Diulia_mod_FW-1	*Dryas iulia moderata*	38,222,516	74.33	12,815,963	33.53
ChIP_input_Diulia_mod_FW-1	*Dryas iulia moderata*	83,903,759	89.01	34,652,243	41.30
ChIP_optix_Diulia_mod_FW-2	*Dryas iulia moderata*	47,329,390	76.6	15,825,011	33.44
ChIP_input_Diulia_mod_FW-2	*Dryas iulia moderata*	97,159,324	89.12	39,356,742	40.51

Hi-C

Sample Name	Species	Sequencing Depth (PE reads)	% paired (alignable)	Hi-C contacts	Pair Type (L-I-O-R)
HiC-Hera_lat_FW-1	*Heliconius erato lativitta*	316,272,331	44.74	68,960,567	25-25-25-25
HiC-Hera_lat_HW-1	*Heliconius erato lativitta*	429,180,982	49.22	105,582,944	25-25-25-25
HiC-Hera_lat_FW-2	*Heliconius erato lativitta*	91,541,201	67.37	35,869,977	25-25-25-25
HiC-Hera_lat_HW-2	*Heliconius erato lativitta*	50,785,849	67.36	16,651,123	25-25-25-25

Sample Name	Inter-scaffold	Intra-scaffold	Short Range	Long Range
HiC-Hera_lat_FW-1	43,694,096	24,451,477	6.00%	11.66%
HiC-Hera_lat_HW-1	58,035,220	47,547,724	8.07%	15.09%
HiC-Hera_lat_FW-2	24,472,626	11,397,351	7.97%	10.95%
HiC-Hera_lat_HW-2	10,823,685	5,827,438	7.64%	10.00%

* Published in Lewis and Reed, 2018

Table S2. CRISPR sgRNA sequences and pools.

Target	sgRNA name	sgRNA pool*	sgRNA sequence
U1	kr29	U1-1	CCGCUCUACUUUACUUUAUU
U1	kr31	U1-1	AUCUUGUAAGUUACAUGGUC
U1	u1p1	U1-1	GGCUCGGUGCAAUUAAUAAA
U1	u1p4	U1-1	GUAUUAUUCAGGACAUGGCU
obs132	obs132_131529F	obs132-1	GAUCACUAACAGUUUUUGCG
obs132	obs132_132061R	obs132-1	GACACACGCUUGUGUAUGUG
obs132	obs132_132244F	obs132-1	AACACGCAUAGUGAACACCA
obs132	obs132_132476F	obs132-1	GGUAGGCACAGGGUAGCACG
obs132	obs132_132902R	obs132-2	AGUGGUCGGUACGCUUGGGU
obs132	obs132_133271F	obs132-2	GGACUAGGGCAGACAAAUAC
obs132	obs132_133512F	obs132-2	UGGCGUCGUAGAGACUAAAC
LR1	LR1_169071F	LR1-1	AGCACCAAGUACACACCUAA
LR1	LR1_169306R	LR1-1	AUACACGCUCGAGGAUAAAA
LR1	LR1_169382F	LR1-2	GCCGUUAAUGGCCGCCUUGG
LR1	LR1_169453F	LR1-2	CUGUUUGUAGGAUAGUGAGG
LR1	LR1_169590F	LR1-2	UCGUAAUUUAGUCCCCCAAC
LR2	LR2_174864F	LR2-1	UGGAUCCCCAUCGAUGCAAA
LR2	LR2_174906F	LR2-1	AAGUGGUGGUAGUAAUACUG
LR2	LR2_175036R	LR2-1	GUUGGCACCAAAGUAACUGG
LR2	kr22	LR2-2	AAAAGGGACCGAAUCUAUGA
LR2	kr23	LR2-2	ACCGACCCUGAACUGAACGC
LR2	kr25	LR2-2	CCACUAAAAUUAACAUCACA
LR2	kr26	LR2-2	GCAACUAUUAAUAAUAUAAA
obs214	obs214_213888F	obs214-1	UUUGGACCACGACGACCUCA
obs214	obs214_214284F	obs214-1	UCAUUUACAAAGGUGCCUUU
obs214	obs214_214410R	obs214-1	GUAGGUGUAAUAGCGGGGCG
obs214m	obs214m_821642F	obs214m-1	ACUAGGGGUAUCAUUUACAA
obs214m	obs214m_821752F	obs214m-1	UCAGUUACAGGAUUGGCUGG
obs214m	obs214_214410R	obs214m-1	GUAGGUGUAAUAGCGGGGCG

*: sgRNA pools are graphically illustrated relative to ATAC and ChIP peaks in fig. S4.

Table S3. CRISPR injections, hatch rate, and efficiency.

Locus	sgRNA pool	Eggs injected	Eggs hatched	Hatch success	Total adults	Adults with wing phenotypes	Adult phenotype efficiency
U1	U1-1	289	180	62%	95	3	3%
obs132	obs132-1	190	47	25%	9	6	67%
obs132	obs132-2	53	10	19%	3	1	33%
LR1	LR1-1	109	23	21%	7	3	43%
LR1	LR1-2	160	19	12%	8	3	38%
LR2	LR2-1	63	19	30%	6	3	50%
LR2	LR2-2	178	~90	51%	42	3	7%
obs214	obs214-1	259	50	19%	8	4	50%
obs214m	obs214m-1	542	unknown	unknown	25	3	12%

Table S4. Descriptions of CRISPR phenotypes for all mutant individuals.

			Phenotype class				
Target	**sgRNA pool**	**Individual**	**Vein**	**Dennis**	**Ray**	**Other**	**Description of phenotypes**
U1	U1-1	U1-29**	x		x		**LVH:** major vein truncation, merging of rays; **RVH:** minor vein truncation
U1	U1-1	U1-37*,**	x		x		**LVH:** major vein truncation, merging of rays; **RVH:** minor vein truncation
U1	U1-1	U1-84				x	**LH:** wing deformed, with miniature and lost scales on both D and V
obs132	Obs132-1	132-1_B	x		x	x	**RH:** miniature wing with truncated/merging veins, multiple rays missing
obs132	Obs132-1	132-1_D				x	**RVF:** large clone of missing wing conjugation scales
obs132	Obs132-1	132-1_E			x		**RDH:** black clone in 3rd ray from posterior margin
obs132	Obs132-1	132-1_F			x		**LVH:** black clone in 3rd-to-bottom ray
obs132	Obs132-1	132-1_G				x	**LVH:** anterior margin yellow mostly missing
obs132	Obs132-1	132-1_I*,**	x		x	x	**LVH:** large black clones across wing delete multiple rays, small ectopic vein fragments, anomolous white spot; **LF:** white clones in yellow region
obs132	Obs132-2	132-2_B*,**		x	x		**LVH:** black clones in posterior rays; **RDF:** many black streaks in dennis; **RVF:** black streaks in dennis; **LDF:** black streak in dennis (different than RDF); **LVF:** black clones in dennis
LR1	LR1-1	R1-1_C*,**			x	x	**LDH:** black notches in four posterior rays; **LVH:** 3rd-to-anterior ray almost entirely gone; **RDH:** slight morphology and color changes to conjugation scales near body
LR1	LR1-1	R1-1_D			x		**LDH:** notch in anterior ray
LR1	LR1-1	R1-1_G				x	**LF:** deformed wing with apparent allometric size reduction of dennis region (no obvious color pattern changes)
LR1	LR1-2	R1-2_B			x	x	**LVH:** posterior red basal spot missing; **RDH:** small black clones in posterior rays; **LDF:** white clones in yellow region; **RDF:** white clones in yellow region (different from LDF)
LR1	LR1-2	R1-2_C*,**		x			**LVF:** large black streak in dennis; **RDF:** black clones in posterior dennis
LR1	LR1-2	R1-2_D	x	x			**LF:** CuA2 vein kinked in dennis region, with associated lightening of red pigmentation
LR2	LR2-1	R2-1_C*,**		x			**RDF:** black streaks in dennis
LR2	LR2-1	R2-1_D**			x		**LVH:** missing two anterior rays; **RDH:** many black clones in rays
LR2	LR2-1	R2-1_F		x	x	x	**LDF:** large white clone in yellow region, black streak in dennis; **LDH:** many black clones in rays; **RDH: possibly deformed,** hole in wing (not from handling)
LR2	LR2-2	LR2_8*,**	x		x	x	**LVF:** vein loss; **LVH:** vein loss, ray loss; **LVF:** wing-conjugation scale transformation to wt
LR2	LR2-2	LR2_41		x			**RVF:** loss of pigmentation in dennis clone
LR2	LR2-2	LR2_49	x				**RVF:** vein truncation
obs214	Obs214-1	214-1_A			x	x	**LVH:** black clones on 2nd-to-anterior ray; **LVF:** posterior delamination of wing
obs214	Obs214-1	214-1_D		x			**RDF:** black clone in dennis
obs214	Obs214-1	214-1_E*,**		x	x	x	**LVF:** black clones and streak in dennis; **LVH:** most rays partially blacked out, anterior ray missing
obs214	Obs214-1	214-1_H		x	x		**RDF:** black clones in dennis, unusual distal extension of dennis; **LVF:** ectopic red ray between CuA1 and CuA2 veins
obs214m	obs214m-1	214m-13		x	x		**RDF:** Black clones in dennis; **RDH:** Black clones in proximal rays subelement possibly homologous to dennis in forewing
obs214m	obs214m-1	214m-14		x		x	**RDF:** black clones in dennis, unusual distal extension of dennis; **LDF:** black clones in dennis, unusual distal extension of dennis
obs214m	obs214m-1	214m-16		x		x	**LDF:** unusual distal extension of dennis

L: left; **R:** right; **D:**dorsal; **V:** ventral; **F:** forewing; **H:** hindwing; *: shown in Fig. 3; **: shown in fig. S5

Table S5. PCR primers used for genotyping.

Primer name	Target	Sequence
U1_KRF	*U1*	CGAGCAGTCCGTGATGTGAT
U1_KRR	*U1*	CGATGCGCTAAGTGTTTCGT
132_3F	*obs132*	TGGAGATTTGAACTGGCGCT
132_3R	*obs132*	GATGACGCTAGATCCGCTCC
132_5F	*obs132*	CTTAGCACTGGGCTCTCAGG
132_5R	*obs132*	GCTCCGTCTTCCACCTTAAA
LR1_1F	*LR1*	GGCAGAGAGAACTCAGCGAA
LR1_1R	*LR1*	GACACTCCGTTCAACAGGCA
LR2_2F	*LR2*	AAGATGACACGTACCACAGTGA
LR2_2R	*LR2*	AAGATCGGTTCGGTTTTTCTT
LR2_KRF	*LR2*	CGCCGTTGCAGTAGCTCTAT
LR2_KRR	*LR2*	CGAACCACAGTCACACAACCAG
214_2F	*obs214*	CACTTCATTTCCCCGCTTT
214_2R	*obs214*	GCATACTTCAACTGTGCCACT